Fully-coupled electro-magneto-elastic behavior of unidirectional multiphased composites via finite-volume homogenization

Qiang Chen[a], Weiqiu Chen[b], Guannan Wang[c,*]

[a] LEM3-UMR 7239 CNRS, Arts et Métiers ParisTech Metz, 4 Rue Augustin Fresnel Metz 57078, France
[b] Department of Engineering Mechanics & Key Laboratory of Soft Machines and Smart Devices of Zhejiang Province & Soft Matter Research Center, Zhejiang University, 38 Zheda Road, Hangzhou, 310027, PR China
[c] Department of Civil Engineering, Zhejiang University, 866 Yuhangtang Road, Hangzhou, 310058, PR China

ABSTRACT

The effective and localized electro-magneto-elastic behavior of periodic unidirectional composites is investigated in this work. Instead of adopting the classical micromechanics models or variational principle-based finite-element (FE) techniques, the finite-volume direct averaging micromechanics (FVDAM) is extended to fulfill this task by incorporating fully-coupled electro-magneto-elastic constitutive relations. Consistent with the mathematical homogenization theories, the mechanical displacements and electric/magnetic potentials are partitioned using two-scale expansion involving the macroscopic and fluctuating contributions. The generalized local stiffness matrices are constructed explicitly by relating the surface-averaged tractions, electric displacements, and magnetic inductions to the surface-averaged mechanical displacements and electric/magnetic potentials, followed which the continuity and periodic boundary conditions are applied. The homogenized coefficients and localized stress, electric/magnetic field distributions are validated extensively against the exact generalized Eshelby solution and an in-house FE program, as well as the experimental measurements, where perfect agreements are observed for all cases. The efficiency and convergence of the proposed multiphysics FVDAM (MFVDAM) are tested by comparing the execution time and localized fields as a function of mesh discretization, with the multiphysics FE (MFEM) results as references. Besides, the MFVDAM is encapsulated into the particle swarm optimization algorithm to deduce the optimal fiber volume fraction at which maximum magnetoelectric coupling effect may occur in the composite system with piezomagnetic ceramics reinforced with piezoelectric unidirectional fibers.

1. Introduction

Piezoelectric-piezomagnetic materials find extensive applications in the emerging intelligent technologies and smart structures, such as the micro-/nano-electromechanical systems (MEMS/NEMS). Relative to the monoclinic electromagnetic materials, fibrous composites consisting of electro-magneto-elastic constituents have several advantages in material flexibility, functional directionality, structural integrity and thus receive significant attentions in several fields such as sensing, vibration control, and structural health monitoring. However, a combination of several distinct constituents into one system causes additional complexities in the material interactions and structural integrity, since not only the effective coefficients but also the localized microscopic response needs to be analyzed.

To avoid the time-consuming and laborious experimental measurement of the piezoelectric-piezomagnetic coupling effect (Munalli et al., 2019; Vijay et al., 2018; Xu et al., 2007), several analytical and numerical techniques have been developed to predict the effective coefficients of composites in the past decades. Benefited from the analytical nature and explicit expressions, most of the earlier contributions are based on the classical micromechanics models, such as the Mori-Tanaka model (Dinzart and Sabar, 2011; Hasanzadeh et al., 2019; Kuo and Peng, 2013; Li and Dunn, 1998), composite cylinder assemblage model (Benveniste, 1994), as well as the generalized self-consistent method (Jiang and Cheung, 2001; Tong et al., 2008). Those classical models usually provide reasonably accurate effective properties predictions with fairly easy implementations and thus draw significant attention from the smart-material communities until presently. However, due to the simplified mean-field assumption, those mentioned techniques cannot accurately recover the localized field distributions, which are important indicators of microcracking and damage initiations (Chen and Wang, 2020; Chen et al., 2018c; Wang,

2018). Although a few analytical solutions are generated for electro-magnetic composites under remote loading conditions (Kuo, 2014; Rashidinejad and Shodja, 2019), more advanced computational techniques require the application of more complex boundary conditions.

With the continuous development of computational capabilities and increasing demand for multiscale analysis between structures and materials, there is reviving interest in developing advanced micromechanics models to simulate the sophisticated piezoelectric-piezomagnetic coupling effects on the effective and localized responses of composite materials. For instance, Lee et al. (2005) employed the finite element (FE) technique to study the averaged properties of three-phase piezoelectric-piezomagnetic composites. Chen and Wang (2020) studied the effect of a fully/partially-cracked interface on the stress and electric field re-distributions in unidirectional composites. Bishay et al. (Bishay and Atluri, 2015; Bishay et al., 2014) implemented the Trefftz concept into finite elements and developed the multi-physics computational grains for the analysis of both the effective and localized responses of electro-magneto-elastic composites. Sladek et al. (2017) used the meshless local Petrov-Galerkin (MLPG) technique to generate the effective properties of composites with multifunctional capabilities. Besides the numerical techniques, asymptotic homogenization methods (AHM) were also employed to study the coupled multiphysics behavior of smart heterogeneous materials (Espinosa-Almeyda et al., 2017; Tang and Yu, 2009). What's more, Haghgoo et al. (2019) employed the simplified unit cell method to investigate the effect of piezoelectric interphases on the effective multiphysics composites. Rabczuk et al. (2019) developed a nonlocal operator method based on the variational principle in solving the dynamic eigenvalue problem of electromagnetic solids. The advantage of the nonlocal operator method is directly employing the energy principle and avoiding the mesh entanglement. Each of the aforementioned techniques has unique advantages in simulating the electro-magneto-elastic materials in terms of either the computational efforts or physical capabilities. However, most of the those techniques place more emphasis on the effective coefficients instead of the localized field concentrations under various loading/boundary conditions that should be equally important in predicting possible crack initiations which usually start from the material level.

In this contribution, we employ the finite-volume based micromechanics with multiphysics capabilities to investigate the effective and localized response of composites reinforced with electro-magneto-elastic phases. Initially employed for the fluid mechanics, the finite volume technique was introduced to solid mechanics for analysis of the micromechanical behavior of periodic composites by Pindera and co-workers (Gattu et al., 2008; Khatam and Pindera, 2009), and functionally graded materials (Cavalcante et al., 2007). In contrast with the FE-based technique wherein the minimization of global potential energy in the unit cell with sufficient mesh refinement leads to the ultimate satisfaction of the unit cell's global equilibrium, the finite-volume technique is based on the direct satisfaction of the governing differential equations for every subvolume at each level of mesh refinement (Chen and Pindera, 2020; Chen et al., 2018b, 2018d). The finite-volume theory has been proved to be an attractive alternative to the finite-element technique in micromechanical modeling of piezoelectric composites or magnetostrictive porous materials (Chen et al., 2018a; Chen and Wang, 2018). However, a fully coupled electro-magneto-elastic constitutive relationship has never been implemented into the FVDAM theory.

Starting from the microstructural characterization, repeating unit cells (RUCs) are identified with periodic boundaries. A fully anisotropic electro-magneto-elastic coupled constitutive relation is implemented into each subvolume of the multiphysics FVDAM theory. The multiphysics local stiffness matrices are constructed by relating the surface-averaged conjugated mechanical displacement-tractions and electric/magnetic potential-electric/magnetic flux components. The accuracy of the theory in generating effective and localized responses are validated against the exact solutions under far-field loading conditions and the

finite element simulations. More importantly, the efficiency of the corresponding program relative to the finite-element technique is tested through comparing the mesh discretization, degrees of freedom in the global system of equations, execution time, as well as the sparsities of the global stiffness matrix, where MFVDAM is superior in several perspectives. Finally, the MFVDAM is encapsulated into the particle swarm optimization algorithm to deduce optimal fiber volume fractions where the maximum electro-magneto coupling coefficients may be obtained. The identification procedure is made more precise by circumventing the traditional trial-and-error approach, substantially reducing the computational cost.

The remainder of the paper is organized as follows: Section 2 briefly introduces the theoretical framework of MFVDAM, a 0th-order homogenization theory of fully coupled multiphysics for unidirectional composites. Section 3 derives the generalized Eshelby solutions for piezoelectric-piezomagnetic composites under multiphysics remote loading. The validation and convergence study of the proposed technique is conducted in Section 4, indicating that the MFVDAM is efficient in reducing the mesh discretization and promoting computational efficiency. Finally, the incorporation of the MFVDAM into the particle swarm optimization is illustrated in Section 5. Section 6 concludes this contribution.

2. Multiphysics finite-volume direct averaging micromechanics

In this contribution, the generalized fully coupled electro-magneto-elastic relation is implemented into the FVDAM theory to study the coupling effect of the fibrous composites reinforced with piezoelectric-piezomagnetic constituents. This relation can be described by the generalized Hooke's law (Li and Dunn, 1998):

$$
\begin{aligned}
\sigma_{ij} &= C_{ijkl}\varepsilon_{kl} - e_{kij}E_k - q_{kij}H_k \\
D_i &= e_{ikl}\varepsilon_{kl} + \kappa_{ij}E_j + \alpha_{ij}H_j \\
B_i &= q_{ikl}\varepsilon_{kl} + \alpha_{ij}E_j + \mu_{ij}H_j
\end{aligned}
\tag{1}
$$

where σ_{ij}, D_i and B_i are the stress, electric displacement, and magnetic induction components, respectively, while ε_{ij}, E_i and H_i are the strain components, electric and magnetic field components, respectively. C_{ijkl}, e_{kij}, q_{kij}, as well as κ_{ij}, μ_{ij} and α_{ij} represent the elastic tensor, piezoelectric tensor, piezomagnetic tensor, as well as dielectric, magnetic permeability and electromagnetic tensors, respectively.

Equation (1) is further expressed in matrix and vector notations for an easier implementation into the FVDAM algorithm:

$$
\begin{bmatrix} \sigma \\ D \\ B \end{bmatrix} = Z \begin{bmatrix} \varepsilon \\ -E \\ -H \end{bmatrix}
\tag{2}
$$

where $Z = \begin{bmatrix} C & -e^T & -q^T \\ e & -\kappa & -\alpha^T \\ q & -\alpha & -\mu \end{bmatrix}$.

2.1. Unit cell discretization

The multiphysics FVDAM is a simplified version of the mathematical homogenization theory or the so-called asymptotic homogenization. The latter is based on a systematic asymptotic analysis of periodic media whose response is characterized by governing differential equations with periodically varying coefficients that reflect the spatial variation of the microstructures. The mathematical homogenization theory provides a consistent framework for taking into account the effect of macroscopic strain, electric field, and magnetic field variations in a periodic material whose microstructural scale is characterized by the small parameter ς. Within this framework, the macroscopic and local variations of displacements, electric potential, and magnetic potential are described in a two-scale representation involving the global coordinates x for macroscopically homogeneous composite materials and the local coordinates y for the repeating unit cell, respectively, connected through the small parameter $\varsigma = x/y$ which characterizes the

size of the unit cell. The operator $\partial/\partial x_i$ in the governing differential equations is then replaced by $\frac{\partial}{\partial x} \rightarrow \frac{\partial}{\partial x} + \frac{1}{\varsigma}\frac{\partial}{\partial y}$ which separates the governing differential equations into different orders of ς or scales. Work by Ammen et al. (Ameen et al., 2018) and He and Pindera (2020) provdes insight into the asymptotic homogenization.

The current multiphysics FVDAM formulation is developed following the classical homogenization theory or the so-called 0$^{\text{th}}$ order homogenization theory. Two hypotheses have been made: the microstructural scale is infinitely small relative to the structural dimension. As a result, the strain/electric field/magnetic field gradient is neglected in the local stress/electric displacement/magnetic induction field recovery at lower microstructural scales (Yang et al., 2019; Zhu et al., 2020). The mechanical displacement, electric potential, and magnetic potential in each phase of the microstructure are partitioned into average and fluctuating contributions dependent on the global and local coordinates, $\mathbf{x} = (x_1, x_2, x_3)$ and $\mathbf{y} = (y_1, y_2, y_3)$, respectively, without considering the higher-order terms:

$$u_i^{(q)}(\mathbf{x}, \mathbf{y}) = \bar{\varepsilon}_{ij}x_j + u_i'^{(q)}(\mathbf{x}, \mathbf{y})$$
$$\phi^{(q)}(\mathbf{x}, \mathbf{y}) = -\bar{E}_j x_j + \phi'^{(q)}(\mathbf{x}, \mathbf{y})$$
$$\chi^{(q)}(\mathbf{x}, \mathbf{y}) = -\bar{H}_j x_j + \chi'^{(q)}(\mathbf{x}, \mathbf{y}) \tag{3}$$

which produce local strain, electric field and magnetic field in the form:

$$\varepsilon_{ij}^{(q)} = \bar{\varepsilon}_{ij} + \varepsilon_{ij}'^{(q)} = \bar{\varepsilon}_{ij} + \frac{1}{2}\left(\frac{\partial u_i'}{\partial y_j} + \frac{\partial u_j'}{\partial y_i}\right)^{(q)}$$
$$E_i^{(q)} = \bar{E}_i + E_i'^{(q)} = \bar{E}_i - \frac{\partial \phi'^{(q)}}{\partial y_i}$$
$$H_i^{(q)} = \bar{H}_i + H_i'^{(q)} = \bar{H}_i - \frac{\partial \chi'^{(q)}}{\partial y_i} \tag{4}$$

where , $\bar{E}_i$ and $\bar{H}_i$ are macroscopic strain, electric field, and magnetic field, respectively. $u_i'^{(q)}(i = 1,2,3)$, $\phi'^{(q)}$ and $\chi'^{(q)}$ are displacement, electric potential, and magnetic potential fluctuations of the q-th subvolume, respectively. Using Eq. (4), the following expressions are obtained for the volume-averaged strain, electric field, and magnetic field taken over the analysis domain:

$$\frac{1}{V}\int_V \varepsilon_{ij}dV = \bar{\varepsilon}_{ij} + \frac{1}{V}\int_V \varepsilon_{ij}'dV$$
$$\frac{1}{V}\int_V E_i dV = \bar{E}_i + \frac{1}{V}\int_V E_i'dV$$
$$\frac{1}{V}\int_V H_i dV = \bar{H}_i + \frac{1}{V}\int_V H_i'dV \tag{5}$$

where V denotes the volume fraction of the repeating unit cell. As the fluctuating components are periodic functions on V, the integrals appearing on the righthand side of Eq. (5) are zero, implying the average strain, electric field and magnetic field taken over the RUC are consistent with their definitions.

In the present work, we limit our analysis to unidirectional composites with continuous reinforcements, the response of which may be characterized by periodically repeating material microstructure with two-dimensional periodicity. The actual unit cell microstructure is discretized into quadrilateral subvolumes designated by the index (q), and its location is specified by the subvolume vertices $(y_2^{(p,q)}, y_3^{(p,q)})$ referred to the fixed RUC coordinate system (the fiber direction is denoted as y_1). Following the convention by Cavalcante et al. [23–24], the vertices are numbered in counterclockwise manners starting from the lower-left corner $(y_2^{(1,q)}, y_3^{(1,q)})$ and the faces are numbered in counterclockwise manners with the face F_p defined by the endpoints $(y_2^{(p,q)}, y_3^{(p,q)})$ and $(y_2^{(p+1,q)}, y_3^{(p+1,q)})$ for $p = 1,2,3,4$ such that $p + 1 \overset{yields}{\rightarrow} p$ when $p = 4$. The qth subvolume is generated by mapping the square-sided subvolume in the reference coordinates $(\eta - \xi)$ onto a quadrilateral subvolume resident in the actual microstructure, Fig. 1, using the Q4-type mapping function (Cavalcante et al., 2007):
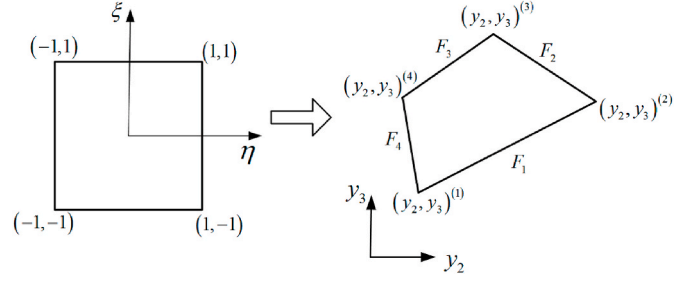

Fig. 1. Parametric mapping of a reference square subvolume in the $\eta - \xi$ coordinate system onto a quadrilateral subvolume in the $y_2 - y_3$ coordinate of the actual microstructure.

$$y_i^{(q)}(\mathbf{x}, \mathbf{y}) = \sum_{p=1}^{4} N_p(\eta, \xi)y_i^{(p,q)}, \quad i = 2,3 \tag{6}$$

where $N_p(\eta, \xi)$ is the shape function given by:

$$N_1(\eta, \xi) = \tfrac{1}{4}(1 - \eta)(1 - \xi), \quad N_2(\eta, \xi) = \tfrac{1}{4}(1 + \eta)(1 - \xi)$$
$$N_3(\eta, \xi) = \tfrac{1}{4}(1 + \eta)(1 + \xi), \quad N_4(\eta, \xi) = \tfrac{1}{4}(1 - \eta)(1 + \xi) \tag{7}$$

2.2. Generalized local stiffness matrix

The fluctuating displacements $u_i'^{(q)}(i = 1,2,3)$, electric potential $\phi'^{(q)}$ and magnetic potential $\chi'^{(q)}$ in the qth subvolume are approximated using the following polynomial expansion in the reference coordinates $(\eta - \xi)$:

$$u_i'^{(q)} = W_{i(00)}^{(q)} + \eta W_{i(10)}^{(q)} + \xi W_{i(01)}^{(q)} + \tfrac{1}{2}(3\eta^2 - 1)W_{i(20)}^{(q)} + \tfrac{1}{2}(3\xi^2 - 1)W_{i(02)}^{(q)}$$
$$\phi'^{(q)} = W_{4(00)}^{(q)} + \eta W_{4(10)}^{(q)} + \xi W_{4(01)}^{(q)} + \tfrac{1}{2}(3\eta^2 - 1)W_{4(20)}^{(q)} + \tfrac{1}{2}(3\xi^2 - 1)W_{4(02)}^{(q)}$$
$$\chi'^{(q)} = W_{5(00)}^{(q)} + \eta W_{5(10)}^{(q)} + \xi W_{5(01)}^{(q)} + \tfrac{1}{2}(3\eta^2 - 1)W_{5(20)}^{(q)} + \tfrac{1}{2}(3\xi^2 - 1)W_{5(02)}^{(q)} \tag{8}$$

where $W_{.(..)}^{(q)}$ are the unknown microvariables associated with each subvolume, which ensure that $\bar{\varepsilon}_{11} = \bar{\varepsilon}_{11}^{(q)}$, $\bar{E}_1 = \bar{E}_1^{(q)}$ and $\bar{H}_1 = \bar{H}_1^{(q)}$ due to the continuous reinforcement in x_1 direction.

Considering the above polynomial expansion, the surface-averaged fluctuating mechanical displacements, electric potential, and magnetic potential on the pth face of qth quadrilateral subvolume are evaluated by (the superscript q is omitted for convenience):

$$\hat{u}_i'^{(1,3)} = \tfrac{1}{2}\int_{-1}^{+1} u_i'(\eta, \mp 1)d\eta \quad \hat{u}_i'^{(2,4)} = \tfrac{1}{2}\int_{-1}^{+1} u_i'(\pm 1, \xi)d\xi$$
$$\hat{\phi}'^{(1,3)} = \tfrac{1}{2}\int_{-1}^{+1} \phi'(\eta, \mp 1)d\eta \quad \hat{\phi}'^{(2,4)} = \tfrac{1}{2}\int_{-1}^{+1} \phi'(\pm 1, \xi)d\xi$$
$$\hat{\chi}'^{(1,3)} = \tfrac{1}{2}\int_{-1}^{+1} \chi'(\eta, \mp 1)d\eta \quad \hat{\chi}'^{(2,4)} = \tfrac{1}{2}\int_{-1}^{+1} \chi'(\pm 1, \xi)d\xi \tag{9}$$

Similar to Eq. (9), the surface-averaged interfacial tractions, normal electric displacements and normal magnetic induction components are defined by:

$$\hat{t}_i^{(1,3)} = \tfrac{1}{2}\int_{-1}^{+1} t_i(\eta, \mp 1)d\eta \qquad \hat{t}_i^{(2,4)} = \tfrac{1}{2}\int_{-1}^{+1} t_i(\pm 1, \xi)d\xi$$
$$\hat{D}_n^{(1,3)} = \tfrac{1}{2}\int_{-1}^{+1} D_n(\eta, \mp 1)d\eta \qquad \hat{D}_n^{(2,4)} = \tfrac{1}{2}\int_{-1}^{+1} D_n(\pm 1, \xi)d\xi$$
$$\hat{B}_n^{(1,3)} = \tfrac{1}{2}\int_{-1}^{+1} B_n(\eta, \mp 1)d\eta \qquad \hat{B}_n^{(2,4)} = \tfrac{1}{2}\int_{-1}^{+1} B_n(\pm 1, \xi)d\xi \tag{10}$$

where $t_i = \sigma_{ji}n_j$, $D_n = D_j n_j$ and $B_n = B_j n_j$. $[n_2, n_3]$ is the unit normal vector that defines the orientations of the surfaces of a given quadrilateral subvolume.

The surface-averaged interfacial tractions, electric displacements, and magnetic inductions in Eq. (10) may be expressed in terms of the surface-averaged mechanical displacements, electric potential, and magnetic potential in Eq. (9) through the generalized local stiffness matrices. Towards this end, we first express the 25 unknown coefficients $W_{.(..)}^{(q)}$ in terms of the surface-averaged mechanical displacements, electric potential, and magnetic potential. The definition in Eq. (9)

provides 20 relations, which relates the first- and second-order coefficients $W_{.(10)}^{(q)}$, $W_{.(01)}^{(q)}$ and $W_{.(20)}^{(q)}$, $W_{.(02)}^{(q)}$ to the surface-averaged mechanical displacements, electric potential, magnetic potential as well as the zeroth-order coefficients $W_{.(00)}^{(q)}$. The determination of the zeroth-order coefficients $W_{.(00)}^{(q)}$ within each subvolume requires 5 additional equations, which are obtained through the application of equilibrium equations and Maxwell equation in the large within each subvolume:

$$\frac{1}{V}\int_V \frac{\partial \sigma_{ij}}{\partial x_j}dV = 0, \quad \frac{1}{V}\int_V \frac{\partial D_i}{\partial x_i}dV = 0, \quad \frac{1}{V}\int_V \frac{\partial B_i}{\partial x_i}dV = 0 \tag{11}$$

This eventually leads to a local system of equations which is symbolically expressed as:

$$\hat{\mathbf{Y}}^{(q)} = \mathbf{K}^{(q)}\hat{\mathbf{U}}^{(q)} + \mathbf{N}^{(q)}\mathbf{Z}^{(q)}\bar{\mathbf{X}} \tag{12}$$

where $\hat{\mathbf{Y}}^{(q)} = [\hat{\mathbf{p}}^{(1)} \quad \hat{\mathbf{p}}^{(2)} \quad \hat{\mathbf{p}}^{(3)} \quad \hat{\mathbf{p}}^{(4)}]^{(q)\mathrm{T}}$, $\hat{\mathbf{p}}^{(p,q)} = [\hat{t}_1 \quad \hat{t}_2 \quad \hat{t}_3 \quad \hat{D}_n \quad \hat{B}_n]^{(p,q)\mathrm{T}}$, $\hat{\mathbf{U}}^{(q)} = [\hat{\mathbf{u}}'^{(1)} \quad \hat{\mathbf{u}}'^{(2)} \quad \hat{\mathbf{u}}'^{(3)} \quad \hat{\mathbf{u}}'^{(4)}]^{(q)\mathrm{T}}$, $\hat{\mathbf{u}}'^{(p,q)} = [\hat{u}_1' \quad \hat{u}_2' \quad \hat{u}_3' \quad \hat{\phi}' \quad \hat{\chi}']^{(p,q)\mathrm{T}}$, $\bar{\mathbf{X}} = [\bar{\varepsilon}_{11} \quad \bar{\varepsilon}_{22} \quad \bar{\varepsilon}_{33} \quad 2\bar{\varepsilon}_{23} \quad 2\bar{\varepsilon}_{13} \quad 2\bar{\varepsilon}_{12} \quad -\bar{E}_1 \quad -\bar{E}_2 \quad -\bar{E}_3 \quad -\bar{H}_1 \quad -\bar{H}_2 \quad -\bar{H}_3]^{\mathrm{T}}$,

$$\mathbf{N}^{(q)} = [\mathbf{n}^{(1)} \quad \mathbf{n}^{(2)} \quad \mathbf{n}^{(3)} \quad \mathbf{n}^{(4)}]^{(q)\mathrm{T}}, \quad \mathbf{n}^{(p,q)} = \begin{bmatrix} 0 & 0 & 0 & n_3 & n_2 & 0 & 0 \\ n_2 & 0 & n_3 & 0 & 0 & 0 & 0 \\ 0 & n_3 & n_2 & 0 & 0 & 0 & 0 \\ 0 & 0 & 0 & 0 & 0 & n_2 & n_3 \end{bmatrix}^{(p,q)}.$$

The generalized local stiffness matrices $\mathbf{K}^{(q)}$ are given explicitly by the subvolume geometry and material properties.

2.3. Global stiffness matrix

The unknown interfacial surface-averaged displacements, electric potential, and magnetic potential are determined by solving a global system of equations generated by first imposing traction, electric displacement, and magnetic induction continuity conditions at common faces of adjacent subvolumes, followed by direct enforcement of fluctuating mechanical displacement, electric potential, and magnetic potential continuity conditions. The resulting global system of equations can be symbolically represented by:

$$\mathbb{K}\hat{U}' = \Delta\mathbb{Z}\bar{X} \tag{13}$$

where $\mathbb{K}$ denotes the generalized global stiffness matrix, the vector $\hat{U}'$ is comprised of all unknown interfacial mechanical displacements, electric potentials, and magnetic potentials. The matrix $\Delta\mathbb{Z}$ represents the differences in the generalized local stiffness matrices of adjacent subvolumes.

2.4. Homogenization

Solution of the global system of equations, Eq. (13), produces the surface-averaged quantities $\hat{U}'$. Thus, the generalized Hill's electro-magneto-elastic concentration matrices $\mathbf{A}^{(q)}$ for the qth subvolume is generated to relate the average strain, electric field and magnetic field to the macroscopic loading vectors (Chen et al., 2018a; Chen and Wang, 2018):

$$\bar{\mathbf{X}}^{(q)} = \mathbf{A}^{(q)}\bar{\mathbf{X}} \tag{14}$$

where the elements of the concentration matrix are determined by applying one component of the macroscopic strains, electric or magnetic fields at a time. Subsequently, the averaged macroscopic stresses, electric displacement and magnetic induction components for each RUC with a volume of V are calculated as:

$$\bar{\sigma} = \frac{1}{V}\int\sigma(\mathbf{x})dV = \frac{1}{V}\sum_{q=1}^{N_q}\int_{V_q}\sigma^{(q)}(\mathbf{x})dV^{(q)} = \sum_{q=1}^{N_q}v^{(q)}\bar{\sigma}^{(q)}$$

$$\bar{\mathbf{D}} = \frac{1}{V}\int\mathbf{D}(\mathbf{x})dV = \frac{1}{V}\sum_{q=1}^{N_q}\int_{V_k}\mathbf{D}^{(k)}(\mathbf{x})dV^{(q)} = \sum_{q=1}^{N_q}v^{(q)}\bar{\mathbf{D}}^{(q)}$$

$$\bar{\mathbf{B}} = \frac{1}{V}\int\mathbf{B}(\mathbf{x})dV = \frac{1}{V}\sum_{q=1}^{N_q}\int_{V_k}\mathbf{B}^{(q)}(\mathbf{x})dV^{(q)} = \sum_{q=1}^{N_q}v^{(q)}\bar{\mathbf{B}}^{(q)} \tag{15}$$

where V_q and $v^{(q)}$ are the volume and volume fraction of the qth

	CoFe$_2$O$_4$	BaTiO$_3$	PZT-7A
C_{11}/GPa	269.1	162	131
C_{12}/GPa	169.6	77.99	74.2
C_{13}/GPa	169.6	77.99	74.2
C_{22}/GPa	285.7	166	148
C_{23}/GPa	172.7	76.97	76.2
C_{33}/GPa	285.7	166	148
C_{44}/GPa	56.49	44.5	35.9
C_{55}/GPa	45.3	43	25.3
C_{66}/GPa	45.3	43	25.3
e_{11}/Cm^{-2}	0	18.6	10.99
e_{12}/Cm^{-2}	0	−4.4	−2.324
e_{26}/Cm^{-2}	0	11.6	9.31
q_{11}/Cm^{-2}	699.7	0	0
q_{12}/Cm^{-2}	580.3	0	0
q_{26}/Cm^{-2}	550	0	0
κ_{11}/nCV^{-1}m^{-1}	−0.093	−12.6	2.081
κ_{22}/nCV^{-1}m^{-1}	−0.08	−11.2	3.984
α_{11}/nCV^{-1}m^{-1}	0	0	0
α_{22}/nCV^{-1}m^{-1}	0	0	0
μ_{11}/nCV^{-1}m^{-1}	−157	−10	0
μ_{22}/nCV^{-1}m^{-1}	590	−5	0

subvolume. Implementation of the localization equations, Eq. (14), and the volume-averaged constitutive relation in each subvolume yields the effective constitutive relations for the multiphase electro-magneto-elastic fibrous composites:

$$\begin{bmatrix} \bar{\sigma} \\ \bar{\mathbf{D}} \\ \bar{\mathbf{B}} \end{bmatrix} = \mathbf{Z}^* \begin{bmatrix} \bar{\varepsilon} \\ -\bar{\mathbf{E}} \\ -\bar{\mathbf{H}} \end{bmatrix} \tag{16}$$

where $\mathbf{Z}^*$ is the effective matrix whose elements are functions of the subvolume geometry, constituent properties, as well as the electro-magneto-elastic concentration matrices. The structure of the matrix $\mathbf{Z}^*$ is expressed as:

$$\mathbf{Z}^* = \begin{bmatrix} \mathbf{C}^* & -\mathbf{e}^{*\mathrm{T}} & -\mathbf{q}^{*\mathrm{T}} \\ \mathbf{e}^* & -\mathbf{\kappa}^* & -\mathbf{\alpha}^{*\mathrm{T}} \\ \mathbf{q}^* & -\mathbf{\alpha}^* & -\mathbf{\mu}^* \end{bmatrix} = \sum_{q=1}^{N_q} v^{(q)}\mathbf{Z}^{(q)}\mathbf{A}^{(q)} \tag{17}$$

After solving the boundary value problems and establishing the effective constitutive equations, the effective electro-magneto-elastic coefficients and localized field distributions can be efficiently generated with the present technique.

3. Electromagnetoelastic eshelby problem

In order to validate the MFVDAM theory, we develop the generalized Eshelby analytical solution for an electromagnetoelastic composite, which describes an infinite piezoelectric-piezomagnetic material that is embedded with a distinct electromagnetic fiber and subjected to transverse far-field electric loading $\bar{D}_2^\infty$ (or magnetic loading $\bar{B}_2^\infty$). Using the transformation relations between the Cartesian and cylindrical coordinates, the boundary conditions at infinity can be applied as:

$$D_r(r \to \infty) = \bar{D}_2^\infty \cos\theta, \; D_\theta(r \to \infty) = -\bar{D}_2^\infty \sin\theta$$
$$\sigma_{zr}(r \to \infty) = 0, \; \sigma_{z\theta}(r \to \infty) = 0$$
$$B_r(r \to \infty) = 0, \; B_\theta(r \to \infty) = 0 \tag{18}$$

The solution of the Eshelby problem for a composite electro-magneto-elastic material that is composed of two different phases starts from the coupled constitutive relation in the cylindrical coordinate:
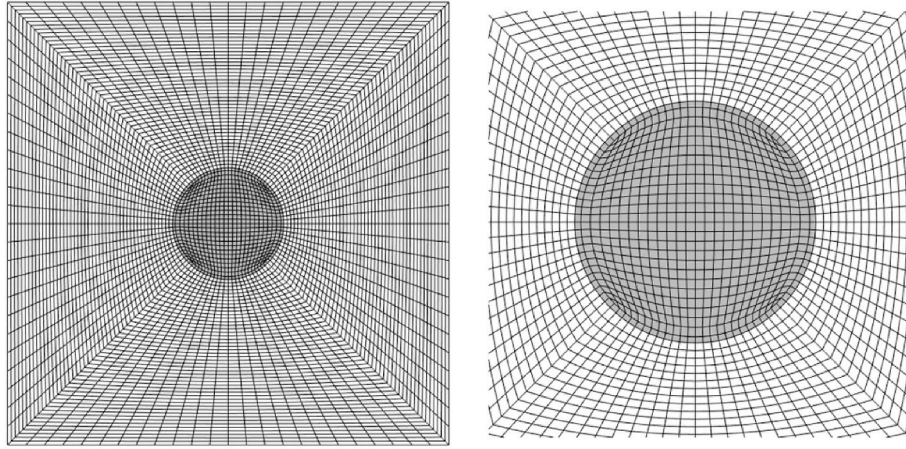
Fig. 2. A repeating unit cell containing 0.05 fiber content in square array and a detailed close-up used for comparison with the generalized Eshelby solution for an inclusion embedded in an infinite matrix.
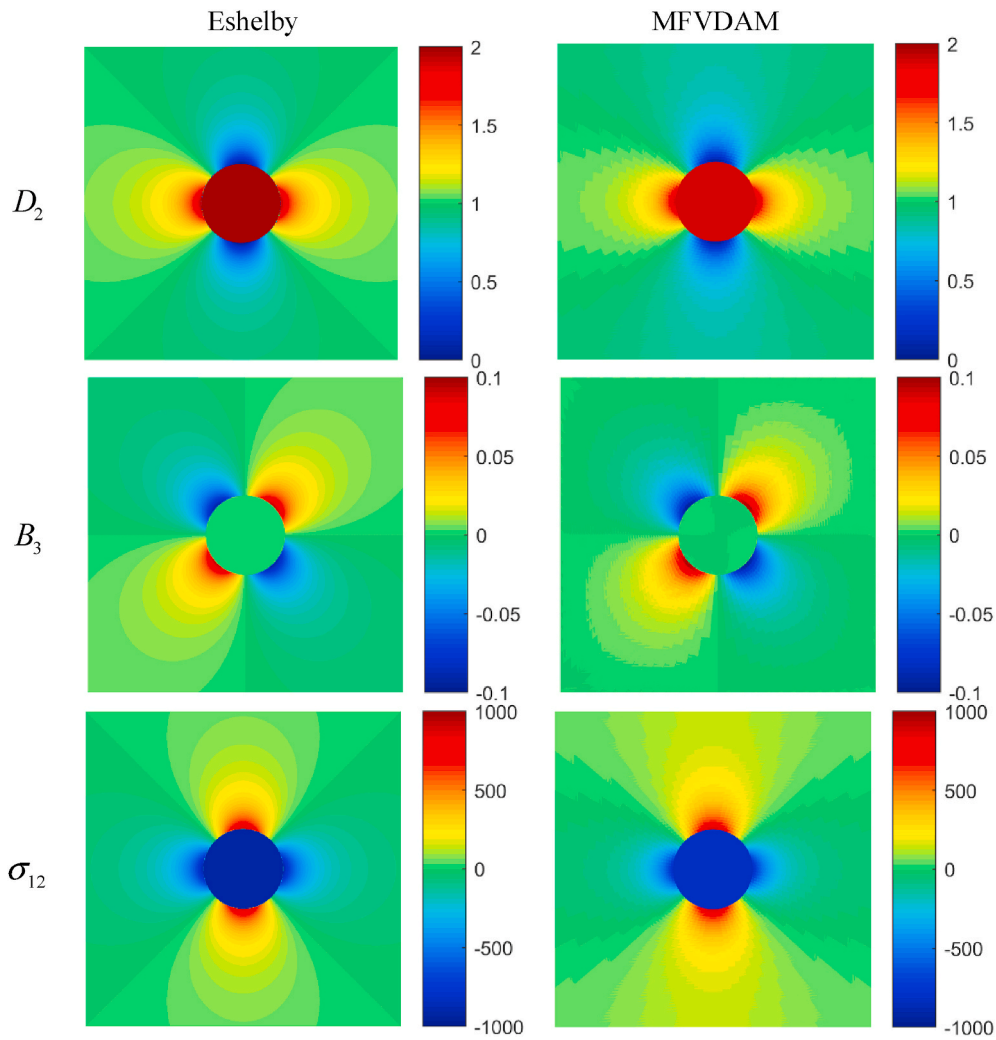

Fig. 3. Comparison of selected local field distribution in the region occupied by the unit cell obtained from the generalized Eshelby and dilute multiphysics FVDAM solutions during far-field loading $D_2^\infty = 1$ C/m^2 condition.
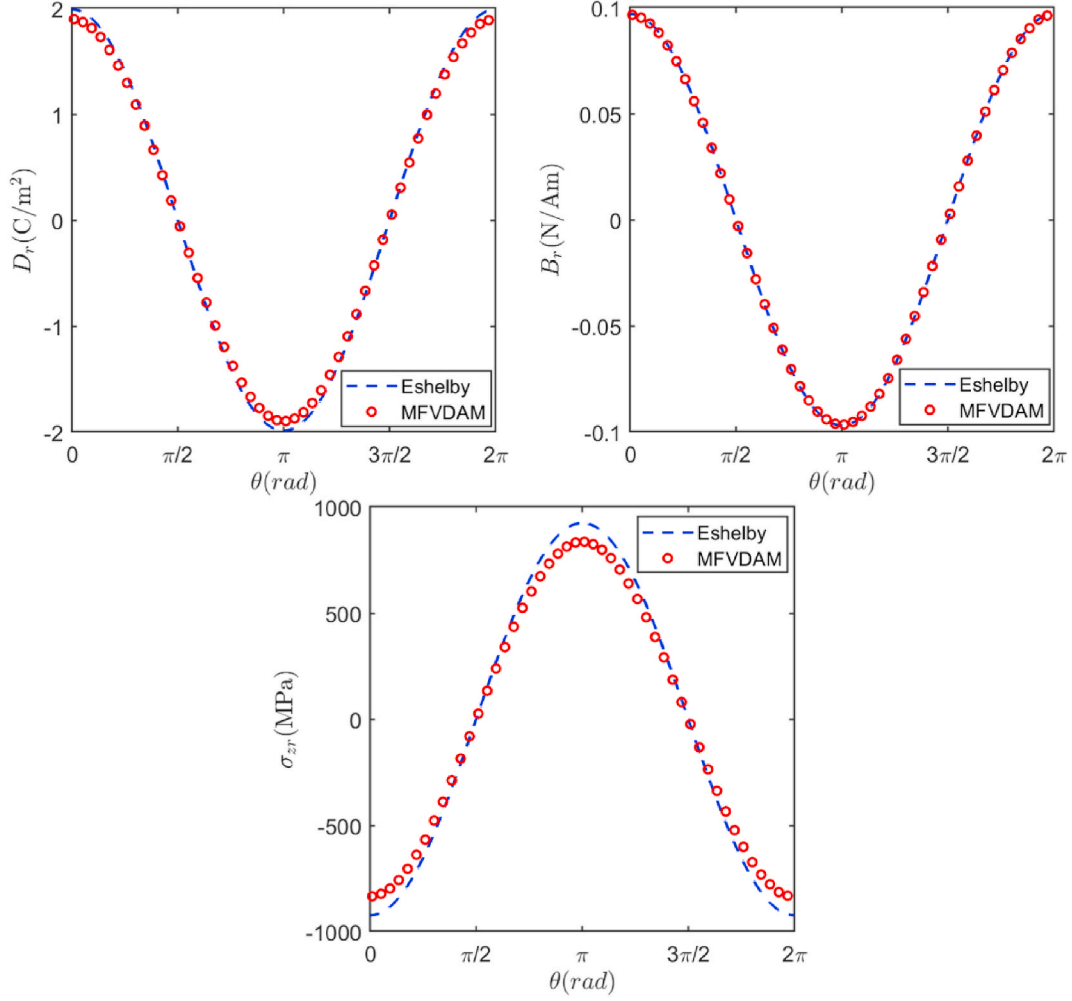
Fig. 4. Comparison of radial electric displacement D_r, magnetic flux density B_r, and shear stress σ_{zr}, around the fiber/matrix interface obtained from the generalized Eshelby and dilute multiphysics FVDAM solutions.

$$
\begin{bmatrix} \sigma_{zr} \\ \sigma_{z\theta} \\ D_r \\ D_\theta \\ B_r \\ B_\theta \end{bmatrix} = \begin{bmatrix} C_{66} & 0 & -e_{15} & 0 & -q_{15} & 0 \\ 0 & C_{66} & 0 & -e_{15} & 0 & -q_{15} \\ e_{15} & 0 & \kappa_{22} & 0 & \alpha_{22} & 0 \\ 0 & e_{15} & 0 & \kappa_{22} & 0 & \alpha_{22} \\ q_{15} & 0 & \alpha_{22} & 0 & \mu_{22} & 0 \\ 0 & q_{15} & 0 & \alpha_{22} & 0 & \mu_{22} \end{bmatrix} \begin{bmatrix} 2\varepsilon_{zr} \\ 2\varepsilon_{z\theta} \\ E_r \\ E_\theta \\ H_r \\ H_\theta \end{bmatrix}
\tag{19}
$$

The stress equilibrium equations and the Maxwell conservation equations read:

$$
\frac{\partial \sigma_{zr}}{\partial r} + \frac{1}{r}\frac{\partial \sigma_{z\theta}}{\partial \theta} + \frac{\sigma_{zr}}{r} = 0
$$
$$
\frac{\partial D_r}{\partial r} + \frac{1}{r}\frac{\partial D_\theta}{\partial \theta} + \frac{D_r}{r} = 0
$$
$$
\frac{\partial B_r}{\partial r} + \frac{1}{r}\frac{\partial B_\theta}{\partial \theta} + \frac{B_r}{r} = 0
\tag{20}
$$

The strain-displacement and electric/magnetic field-electric/magnetic potential relations can be expressed as:

$$
\varepsilon_{zr} = \frac{1}{2}\frac{\partial u_z}{\partial r}, \quad \varepsilon_{z\theta} = \frac{1}{2r}\frac{\partial u_z}{\partial \theta},
$$
$$
E_r = -\frac{\partial \phi}{\partial r}, \quad E_\theta = -\frac{1}{r}\frac{\partial \phi}{\partial \theta},
$$
$$
H_r = -\frac{\partial \chi}{\partial r}, \quad H_\theta = -\frac{1}{r}\frac{\partial \chi}{\partial \theta},
\tag{21}
$$

Substitution of Eq. (21) into Eq. (19) and then into Eq. (20) leads to the generalized equilibrium equation and Maxwell equations in terms of the mechanical displacement, electric and magnetic potentials:

$$
C_{66}\left(\frac{\partial^2 u_z}{\partial r^2} + \frac{\partial u_z}{r\partial r} + \frac{\partial^2 u_z}{r^2\partial\theta^2}\right) + e_{15}\left(\frac{\partial^2 \phi}{\partial r^2} + \frac{\partial \phi}{r\partial r} + \frac{\partial^2 \phi}{r^2\partial\theta^2}\right) + q_{15}\left(\frac{\partial^2 \chi}{\partial r^2} + \frac{\partial \chi}{r\partial r} + \frac{\partial^2 \chi}{r^2\partial\theta^2}\right) = 0
$$
$$
e_{15}\left(\frac{\partial^2 u_z}{\partial r^2} + \frac{\partial u_z}{r\partial r} + \frac{\partial^2 u_z}{r^2\partial\theta^2}\right) - \kappa_{22}\left(\frac{\partial^2 \phi}{\partial r^2} + \frac{\partial \phi}{r\partial r} + \frac{\partial^2 \phi}{r^2\partial\theta^2}\right) - \alpha_{22}\left(\frac{\partial^2 \chi}{\partial r^2} + \frac{\partial \chi}{r\partial r} + \frac{\partial^2 \chi}{r^2\partial\theta^2}\right) = 0
$$
$$
q_{15}\left(\frac{\partial^2 u_z}{\partial r^2} + \frac{\partial u_z}{r\partial r} + \frac{\partial^2 u_z}{r^2\partial\theta^2}\right) - \alpha_{22}\left(\frac{\partial^2 \phi}{\partial r^2} + \frac{\partial \phi}{r\partial r} + \frac{\partial^2 \phi}{r^2\partial\theta^2}\right) - \mu_{22}\left(\frac{\partial^2 \chi}{\partial r^2} + \frac{\partial \chi}{r\partial r} + \frac{\partial^2 \chi}{r^2\partial\theta^2}\right) = 0
\tag{22}
$$

By solving Eq. (22), the solutions for the axial displacement, transverse electric and magnetic potentials are obtained as series expansions:

$$
u_z^i = (H_1^i r + H_3^i/r)\cos\theta + (H_2^i r + H_4^i/r)\sin\theta
$$
$$
\phi^i = (F_1^i r + F_3^i/r)\cos\theta + (F_2^i r + F_4^i/r)\sin\theta
$$
$$
\chi^i = (G_1^i r + G_3^i/r)\cos\theta + (G_2^i r + G_4^i/r)\sin\theta
\tag{23}
$$

for the fiber ($i = f$) and matrix ($i = m$) phases, respectively. It should be pointed out that the higher-order terms are eliminated by comparing the internal functions in Eq. (23) and far-field boundary conditions in Eq. (18) within which only the first-order harmonic terms ($\cos\theta$ and $\sin\theta$) are involved. In addition, we set $H_3^f = H_4^f = F_3^f = F_4^f = G_3^f = G_4^f = 0$ of Eq. (23) since the displacement, electric and magnetic potentials are bounded in the fiber domain.

By employing Eqs. (19) and (21), the corresponding axial shear stress, inplane electric displacement, and magnetic induction are expressed as:
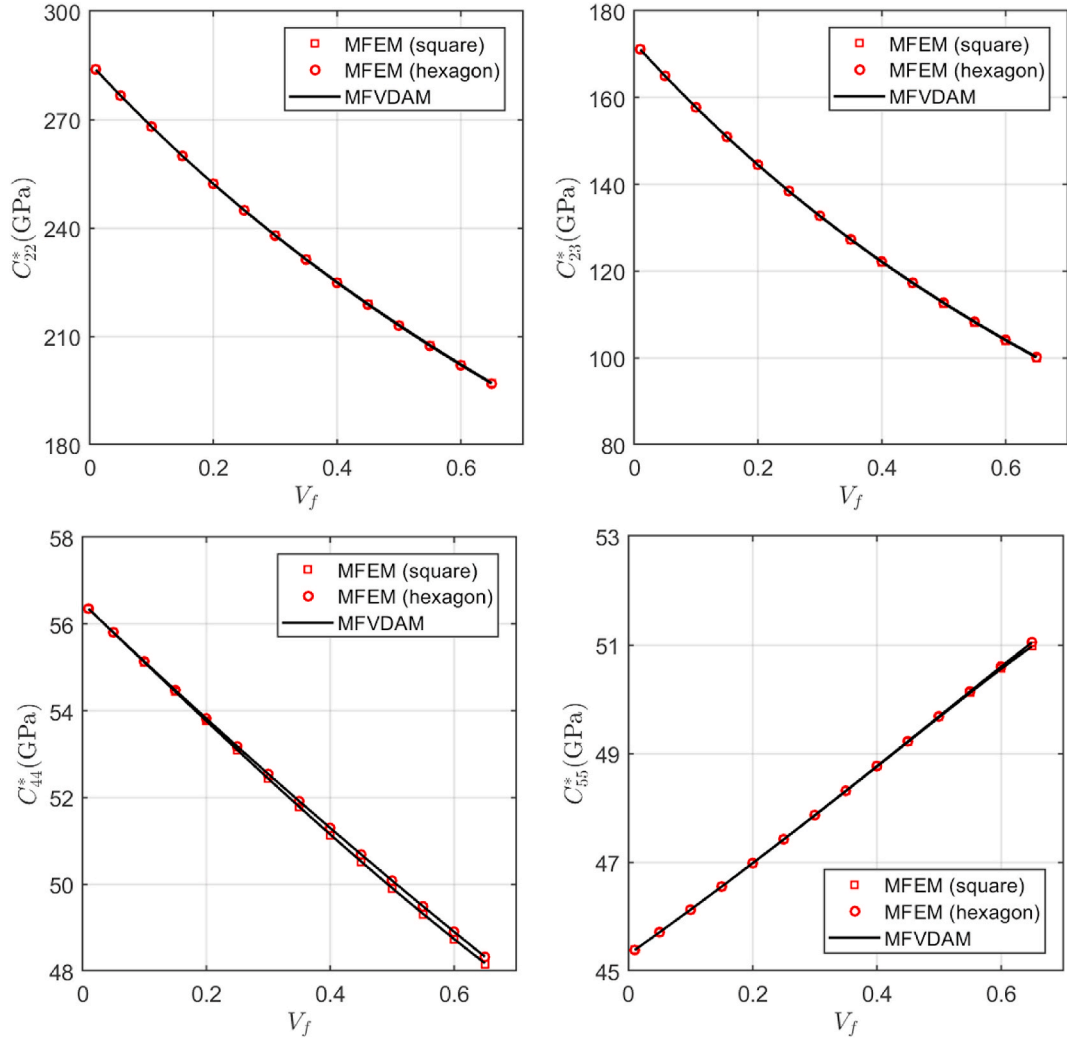
Fig. 5. Selected homogenized elastic moduli of a unidirectional BaTiO$_3$/CoFe$_2$O$_4$ composite as a function of BaTiO3 volume content.

$$
\begin{aligned}
\sigma_{zr}^i &= [(C_{66}^i H_1^i + e_{15}^i F_1^i + q_{15}^i G_1^i) - (C_{66}^i H_3^i + e_{15}^i F_3^i + q_{15}^i G_3^i)r^{-2}]\cos\theta \\
&\quad + [(C_{66}^i H_2^i + e_{15}^i F_2^i + q_{15}^i G_2^i) - (C_{66}^i H_4^i + e_{15}^i F_4^i + q_{15}^i G_4^i)r^{-2}]\sin\theta \\
D_r^i &= [(e_{15}^i H_1^i - \kappa_{22}^i F_1^i - \alpha_{22}^i G_1^i) - (e_{15}^i H_3^i - \kappa_{22}^i F_3^i - \alpha_{22}^i G_3^i)r^{-2}]\cos\theta \\
&\quad + [(e_{15}^i H_2^i - \kappa_{22}^i F_2^i - \alpha_{22}^i G_2^i) - (e_{15}^i H_4^i - \kappa_{22}^i F_4^i - \alpha_{22}^i G_4^i)r^{-2}]\sin\theta \\
B_r^i &= [(q_{15}^i H_1^i - \alpha_{22}^i F_1^i - \mu_{22}^i G_1^i) - (q_{15}^i H_3^i - \alpha_{22}^i F_3^i - \mu_{22}^i G_3^i)r^{-2}]\cos\theta \\
&\quad + [(q_{15}^i H_2^i - \alpha_{22}^i F_2^i - \mu_{22}^i G_2^i) - (q_{15}^i H_4^i - \alpha_{22}^i F_4^i - \mu_{22}^i G_4^i)r^{-2}]\sin\theta
\end{aligned}
\tag{24}
$$

Again, a comparison between Eq. (24) at infinity ($r \to \infty$) and the boundary conditions in Eq. (18) leads to

$$
\begin{aligned}
&C_{66}^m H_1^m + e_{15}^m F_1^m + q_{15}^m G_1^m = 0, \\
&e_{15}^m H_1^m - \kappa_{22}^m F_1^m - \alpha_{22}^m G_1^m = \bar{D}_2^\infty, \\
&q_{15}^m H_1^m - \alpha_{22}^m F_1^m - \mu_{22}^m G_1^m = 0 \\
&H_2^m = F_2^m = G_2^m = 0
\end{aligned}
\tag{25}
$$

The remaining unknown coefficients are solved through applying the continuities at the fiber/matrix interface:

$$
\begin{aligned}
&u_z^f(r=a) = u_z^m(r=a), \quad \sigma_{zr}^f(r=a) = \sigma_{zr}^m(r=a) \\
&\phi^f(r=a) = \phi^m(r=a), \quad D_r^f(r=a) = D_r^m(r=a) \\
&\chi^f(r=a) = \chi^m(r=a), \quad B_r^f(r=a) = B_r^m(r=a)
\end{aligned}
\tag{26}
$$

which leads to the following final system of equations:

$$
\begin{bmatrix}
1 & 0 & 0 & -1/a^2 & 0 & 0 \\
0 & 1 & 0 & 0 & -1/a^2 & 0 \\
0 & 0 & 1 & 0 & 0 & -1/a^2 \\
C_{66}^f & e_{15}^f & q_{15}^f & C_{66}^m/a^2 & e_{15}^m/a^2 & q_{15}^m/a^2 \\
e_{15}^f & -\kappa_{22}^f & -\alpha_{22}^f & e_{15}^m/a^2 & -\kappa_{22}^m/a^2 & -\alpha_{22}^m/a^2 \\
q_{15}^f & -\alpha_{22}^f & -\mu_{22}^f & q_{15}^m/a^2 & -\alpha_{22}^m/a^2 & -\mu_{22}^m/a^2
\end{bmatrix}
\begin{Bmatrix}
H_1^f \\ F_1^f \\ G_1^f \\ H_3^m \\ F_3^m \\ G_3^m
\end{Bmatrix}
$$
$$
=
\begin{bmatrix}
1 & 0 & 0 \\
0 & 1 & 0 \\
0 & 0 & 1 \\
C_{66}^m & e_{15}^m & q_{15}^m \\
e_{15}^m & -\kappa_{22}^m & -\alpha_{22}^m \\
q_{15}^m & -\alpha_{22}^m & -\mu_{22}^m
\end{bmatrix}
\begin{Bmatrix}
H_1^m \\ F_1^m \\ G_1^m
\end{Bmatrix}
\tag{27}
$$

The unknown coefficients can be determined from Eqs. (25) and (27). The solution is employed to validate the present MFVDAM technique in the next section.

4. Numerical results

As explained in Sections 2-3, the MFVDAM enforces volume-averaged equilibrium and conservation equations within each subvolume and adopts surface-averaged continuity conditions between adjacent elements (Fig. 1), while the finite-element methods are based on the variation of total Lagrange multipliers and node-to-node continuities.
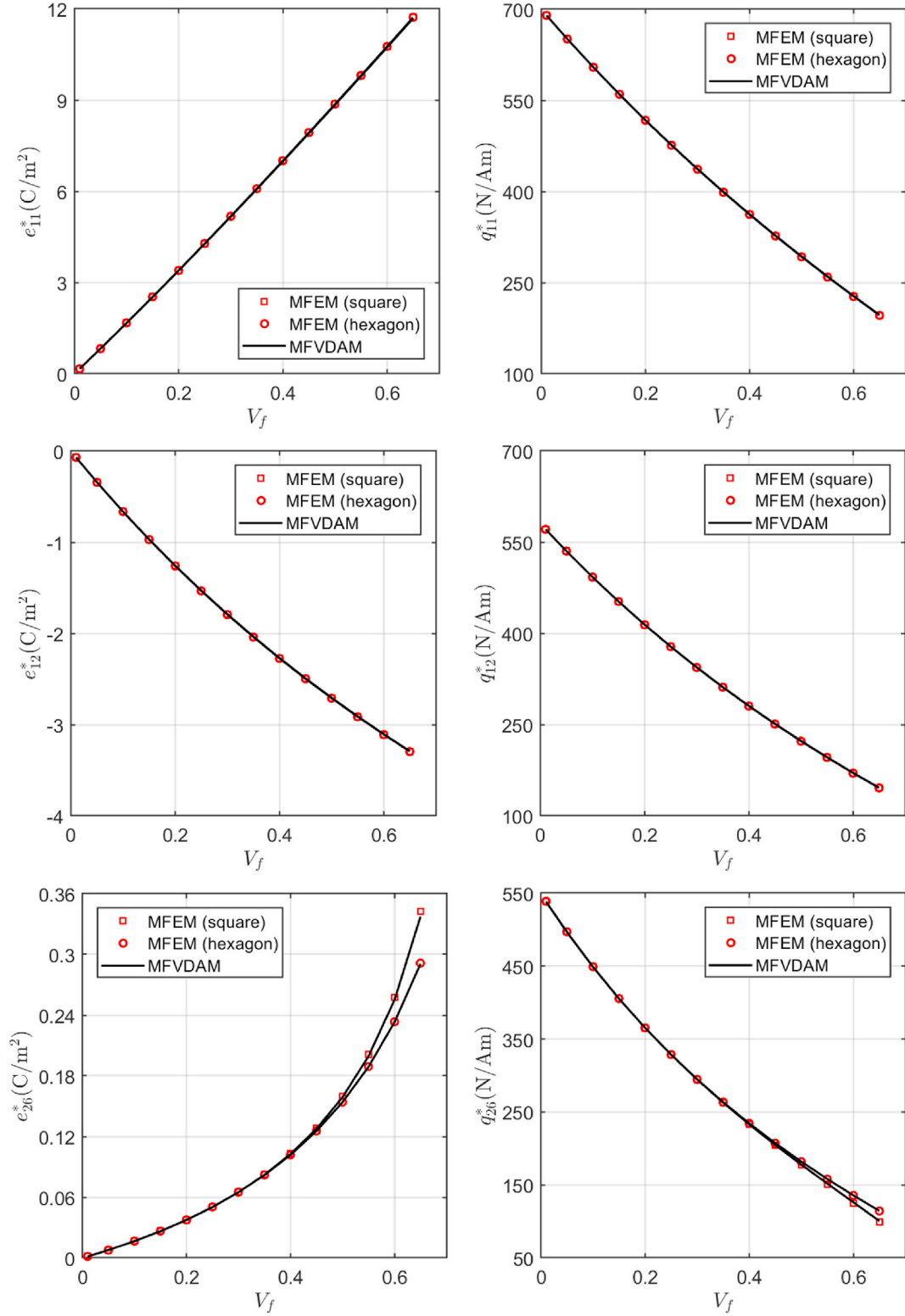
Fig. 6. The effective piezoelectric and piezomagnetic coefficients of a unidirectional $BaTiO_3/CoFe_2O_4$ composite as a function of BaTiO3 volume content.

Hence, the equilibrium equations and conservation equations are not satisfied at the element level in the FE simulation. Validating the FVDAM-generated results against the Multiphysics FEM and Eshelby solutions in both the effective response and localized elastic-electric-magnetic concentrations provides robust credence of the developed MFVDAM results. In the meantime, the computational efficiency and convergence of the present approach relative to the finite-element results are illustrated.

The constituents of the fibrous composites studied in this section are composed of the $CoFe_2O_4$ matrix reinforced with piezoceramic $BaTiO_3$ fibers. The material constants found in the reference (Li and Dunn, 1998) are listed in Table 1. It should be noted that although the
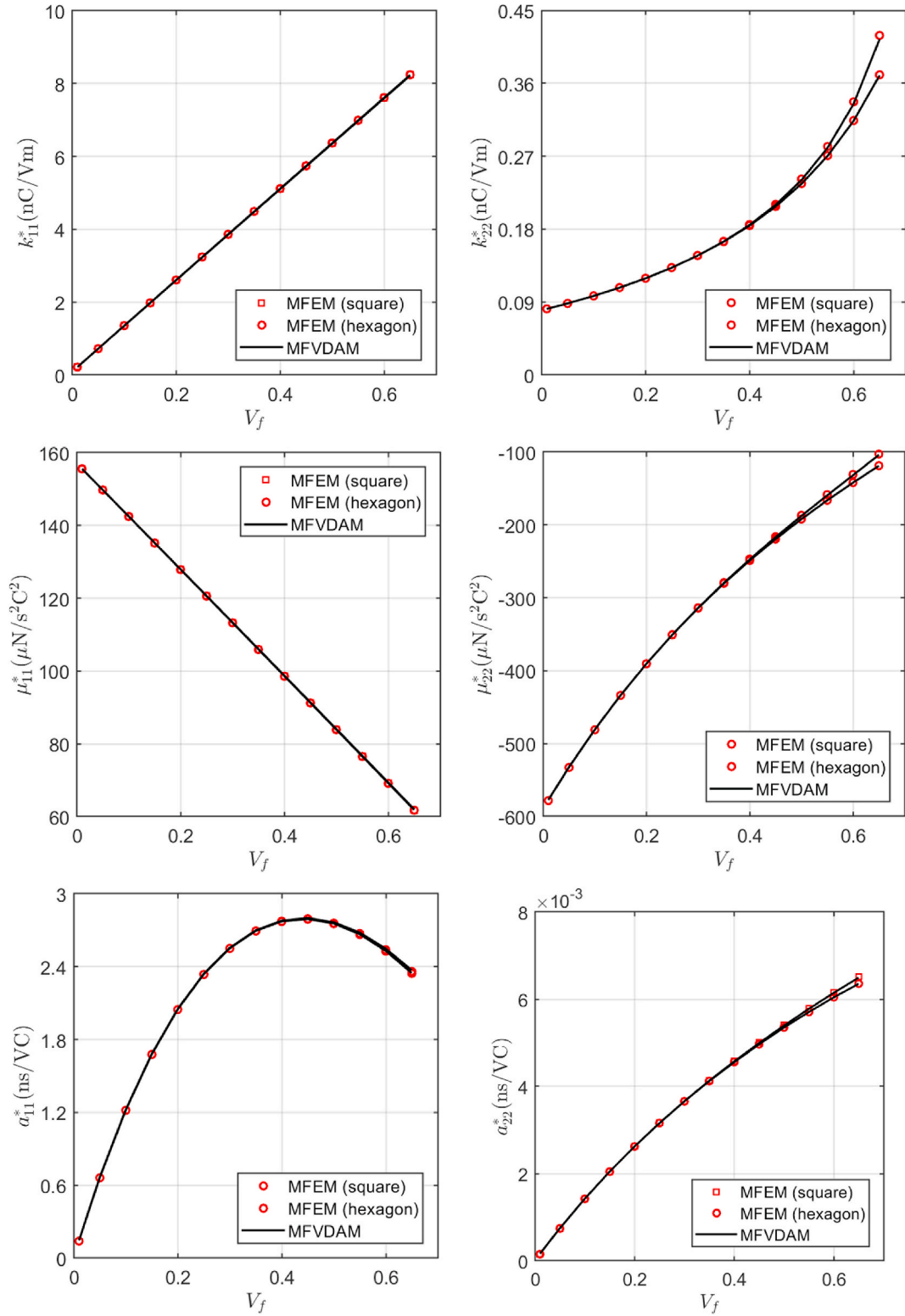
Fig. 7. The dielectric, permeability and electromagnetic coefficients of a unidirectional BaTiO$_3$/CoFe$_2$O$_4$ composite as a function of BaTiO3 volume content.

materials investigated herein are transversely isotropic, the MFVDAM admits fully anisotropic electro-magneto-elastic phases.

4.1. Analytical verification

The multiphysics FVDAM are firstly validated by comparison with the exact solution for a dilute case where an electro-magneto-elastic

fiber is embedded in an infinite matrix which is further subjected to far-field loading conditions. This is the generalized Eshelby problem described in Section 3. To simulate the far-field loading in the analytical solution, a square repeating unit cell with 5% fiber volume fraction is adopted in the MFVDAM simulation. The detailed mesh discretization is illustrated in Fig. 2 with a zoom-in screen of the meshes.

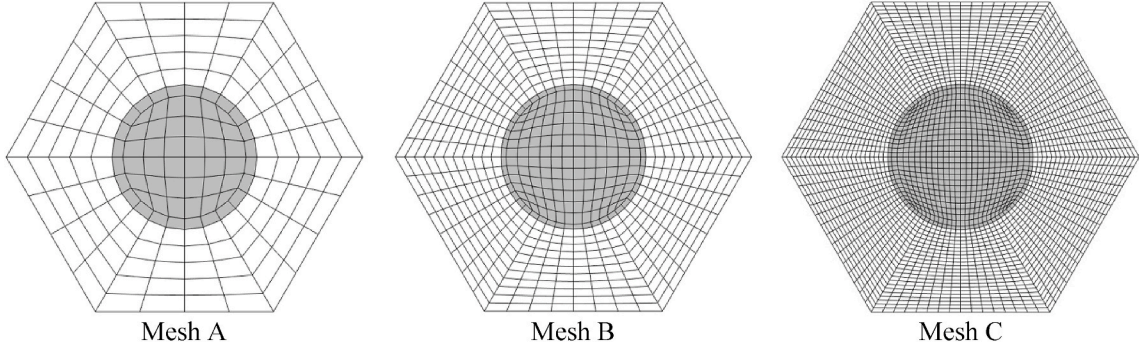In this situation, a far-field unit electric displacement is applied in

Fig. 8. Discretizations of hexagonal unit cells with different mesh refinements.

Table 2
Comparison of the convergence between the present MFVDAM and finite element technique.

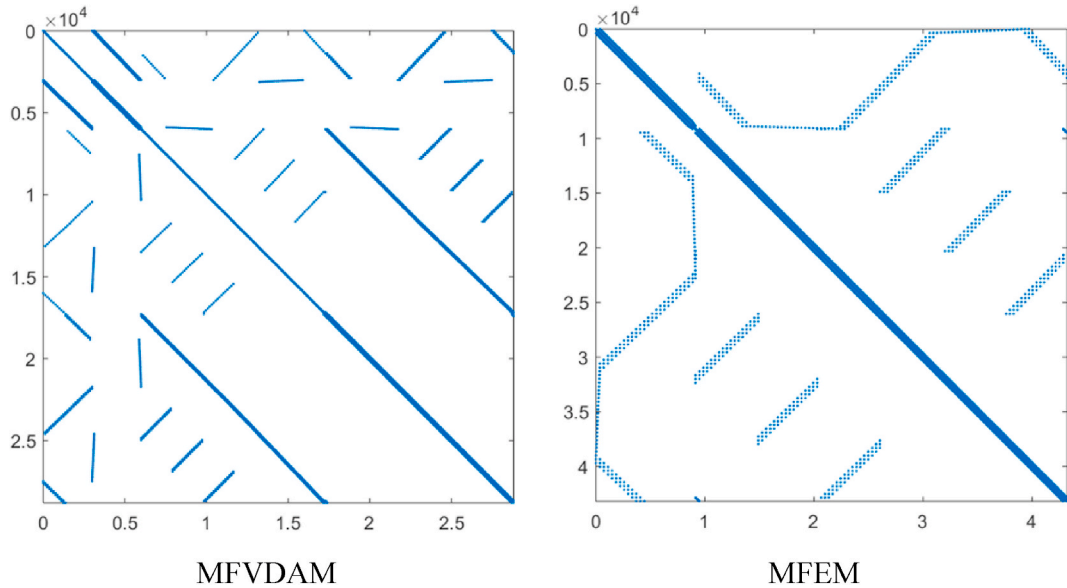| Meshes	Discretization	Degrees of freedom		Nonzero elements		Density		Execution time[a]/s	
		MFVDAM	MFEM	MFVDAM	MFEM	MFVDAM	MFEM	MFVDAM	MFEM
A	180	1800	2700	32376	76430	0.9993%	1.0484%	1.86	4.65
B	720	7200	10800	129271	305174	0.2494%	0.2616%	5.11	53.29
C	2880	28800	43200	516815	1219535	0.0623%	0.0653%	162	846

[a] Averaged based on three runs.

Fig. 9. Nonzero element distributions in the global stiffness matrix for the type-C mesh.

the transverse direction $D_2^\infty = 1\,C/m^2$, where the resultant distributions of electric displacement $D_2(y_2, y_3)$, magnetic induction $B_3(y_2, y_3)$, as well as the axial shear stress component $\sigma_{12}(y_2, y_3)$ are compared between the derived Eshelby solutions and MFVDAM predictions. As observed in Fig. 3, the differences between the two computational approaches are almost invisible. We note that while the magnitude of electric displacement $D_2(y_2, y_3)$ in the fibrous domain is much higher than that in the matrix phase, almost zero values are observed for the magnetic and stress fields in the fiber domain. In a more direct comparison, the converted radial electric displacement $D_r(y_2, y_3)$ and magnetic induction $B_r(y_2, y_3)$, as well as the stress $\sigma_{zr}(y_2, y_3)$ from the Cartesian coordinates are quantitatively compared at the fiber/matrix interface, Fig. 4. The MFVDAM simulation coincides with the exact solution almost everywhere of the entire angular position. A close look at the axial shear stress reveals a slight difference and the stress magnitudes predicted by the Eshelby solutions are slightly larger than the

MFVDAM results. The differences between the elasticity and numerical solutions can be attributed to the applied boundary conditions. While far-field separable loading condition is applied in the former case (Section 3), the periodic boundary conditions are implemented in the latter one (Section 2). We have verified that the difference vanishes when a smaller fiber volume fraction is utilized.

4.2. Numerical verification

After ensuring the accuracy of the localized stress/electric/magnetic field distributions, the MFVDAM-generated effective coefficients are tested against the in-house finite-element results (Chen and Wang, 2020), which provide a gold standard. It is important to point out that the finite-element results have been generated in an uncompiled MATLAB environment that mimics the unit cell solution methodology employed by the multiphysics FVDAM theory, where the mechanical
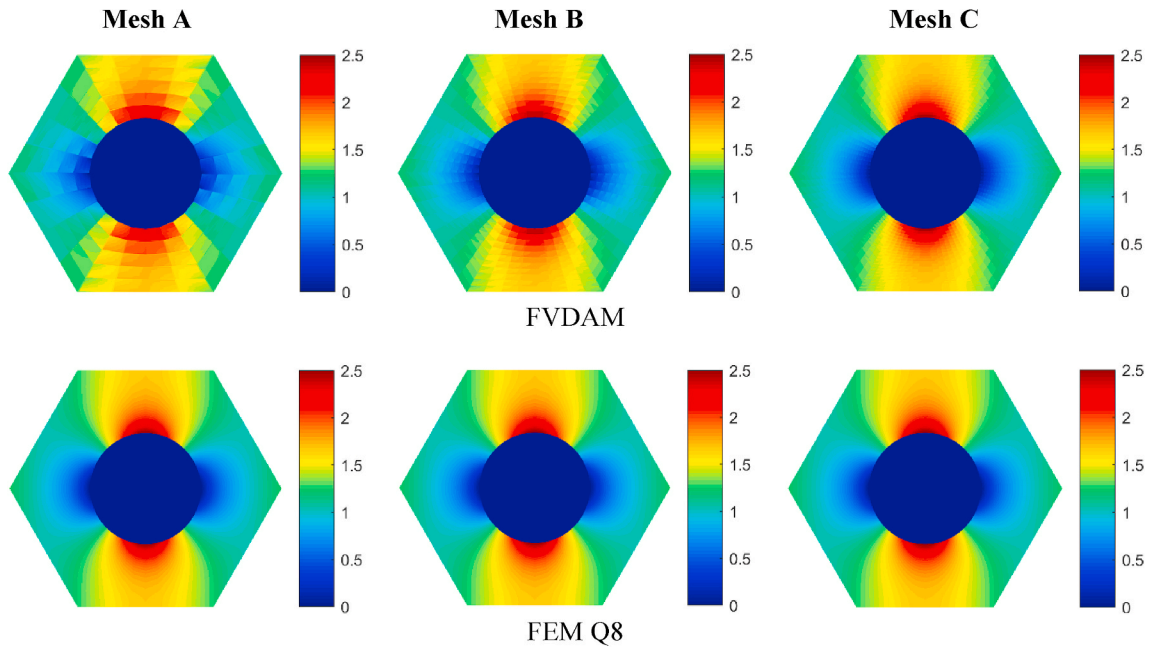
Fig. 10. Comparison of transverse magnetic flux densityB_2 distribution with imposition of unit macroscopic.$\bar{B}_2 = 1$ N/Am
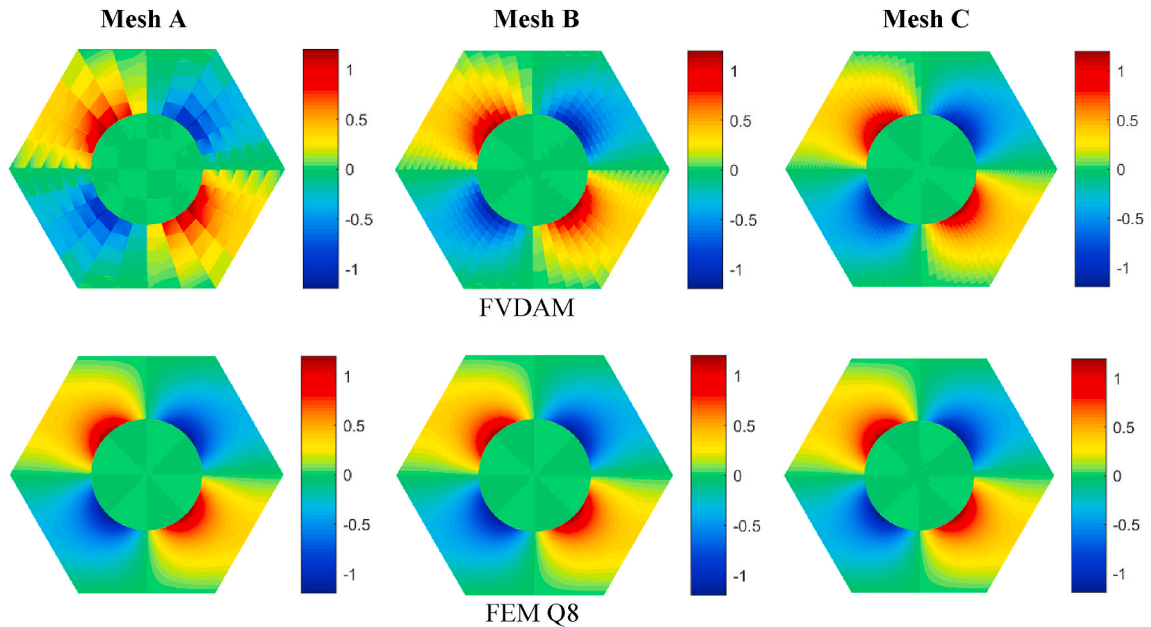

Fig. 11. Comparison of axial shear stress distribution σ_{13} with imposition of unit macroscopic.$\bar{B}_2 = 1$ N/Am

displacements, electric/magnetic potentials are expressed in terms of two-scale expansions and the continuity and periodic boundary conditions are enforced at the common nodes of the adjacent elements. Therefore, the two sets of results may be compared on a one-to-one basis. We note that there are two fundamental differences between the finite-element and multiphysics FVDAM approaches in the manner of satisfying the governing differential equations and applying the continuity and periodicity conditions. Firstly, while the minimization of total potential energy within the finite-element framework leads to the ultimate satisfaction of the unit cell's global equilibrium and conservation with sufficient mesh refinement, the MFVDAM approach enforces equilibrium and conservation in the integral sense for every subvolume at each level of mesh refinement. Secondly, the continuity and periodicity conditions are enforced only on the adjacent nodal displacements and electric/magnetic potentials of the discretized unit

cells in the finite-element approach, whereas the continuity and periodicity conditions are applied on both the surface-averaged tractions, electric displacement, magnetic induction and mechanical displacements, electric/magnetic potentials in the multiphysics finite-volume technique.

First of all, selected homogenized elastic moduli were generated for a BaTiO$_3$/CoFe$_2$O$_4$ material system with both square and hexagonal fiber configurations for fiber volume fractions in the range of $V_f \in [0,0.65]$, Fig. 5. Perfectly matched results are obtained between the finite-element and finite-volume techniques, providing solid credence of the present technique. The selected moduli vary linearly with increasing fiber content, including the transverse normal and shear moduli.

Variations of the effective piezoelectric and piezomagnetic coefficients as a function of fiber content are illustrated in Fig. 6. The
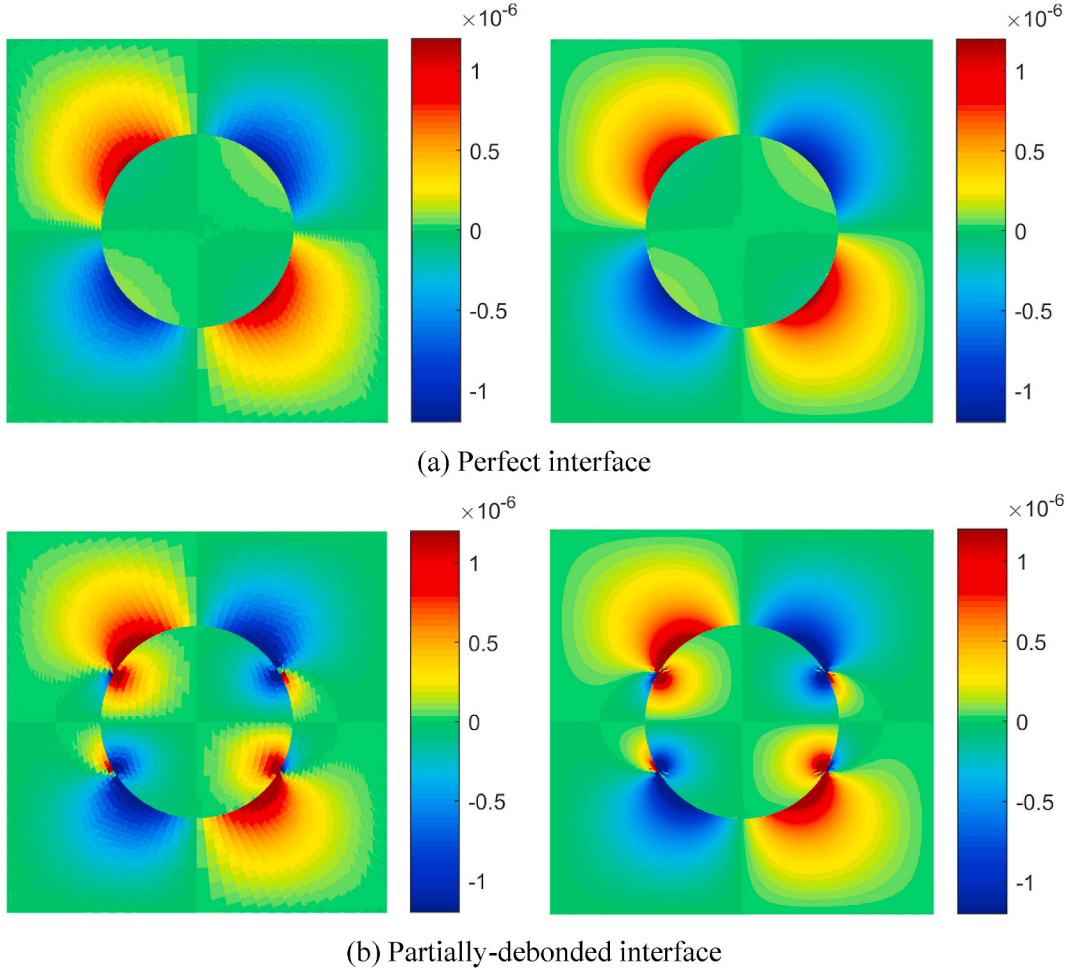
Fig. 12. Effect of interfacial bonding state on the electric displacement D_3 distribution with imposition of unit macroscopic $\bar{B}_2 = 1$ N/Am generated by the MFVDAM (left) and MFEM (right).

piezoelectric/piezomagnetic coefficients are used to measure the conversion between the mechanical energy and the electric/magnetic energy and they are thus important indicators for the energy-converting effect. Accurate prediction of the corresponding coefficients helps to understand the composites' application in the smart structures. Since the BaTiO$_3$ fiber is a piezoelectric material while the CoFe$_2$O$_4$ is a piezomagnetic material, the effective piezoelectric coefficients increase from zeros with the increase of the fiber volume fraction, while the effective piezomagnetic coefficients exhibit an opposite trend.

More interesting results are generated in Fig. 7 for the dielectric, permeability, and electromagnetic coefficients. It is reported in the literature that the coupling electromagnetic coefficients α_{ij}, which are important to indicate the energy conversion between electricity and magnetism, are difficult to obtain for any monoclinic material. However, the present results suggest that the non-zero electromagnetic coefficients can be generated in composite materials even though the corresponding coefficients are zeros in either constituent, Table 1. Once again, the finite-volume and finite-element methods generate highly agreeable results.

It is important to note that the microstructural effect is negligible on either mechanical or electric/magneto properties, especially at low and intermediate volume fractions. This is due to the fact that, for the present material system, the property contrast between the BaTiO$_3$ and CoFe$_2$O$_4$ phases is insignificant. The array effect becomes noticeable at larger fiber-volume fractions where the fiber-fiber interaction is more pronounced. The multiphysics FVDAM is hence consistent with this observation, demonstrating the method is sufficiently sensitive to capture these small effects.

We proceed to test the convergence of the multiphysics FVDAM for generating the local stress/magnetic/electric field distributions as a function of mesh discretization. Three different mesh discretizations are employed with progressively greater refinement. Fig. 8 illustrates the meshes of a hexagonal repeating unit cell with 180, 720, and 2880 subvolumes, respectively, all of which are implemented into the in-house FE programs to generate reference results. The fiber volume fraction is fixed at 0.25 in this simulation. The corresponding degrees of freedom (DOFs) of the three meshes in the two computational approaches are listed in Table 2, where MFVDAM usually consumes two-thirds of the total DOFs by MFEM. Fig. 9 illustrates the non-zero element distribution within the global stiffness matrix for the mesh C discretization. Due to the applied periodic boundary conditions, the global stiffness matrix is sparse but not banded. Therefore, inverting the global stiffness becomes more computationally demanding. The number of non-zero elements in the global system of equations of MFVDAM approach is drastically smaller than that of the MFEM of the same mesh discretization, with a concomitant decrease of density of the nonzero elements in the global system of equations in the case of MFVDAM calculation, hence an improvement in computational efficiency. The execution time by the MFEM and MFVDAM based on three runs are enclosed in Table 2 for comparison. It is demonstrated that the MFVDAM sees a significant reduction in execution time relative to the MFEM in the case of the same mesh discretizations.

What's more, the localized inplane magnetic induction B_2, as well as the out-of-plane shear stress component, σ_{13} are illustrated in Figs. 10 and 11, respectively. Similar to the previous cases, both the MFVDAM and eight-node FEM elements are employed for comparison. Due to the
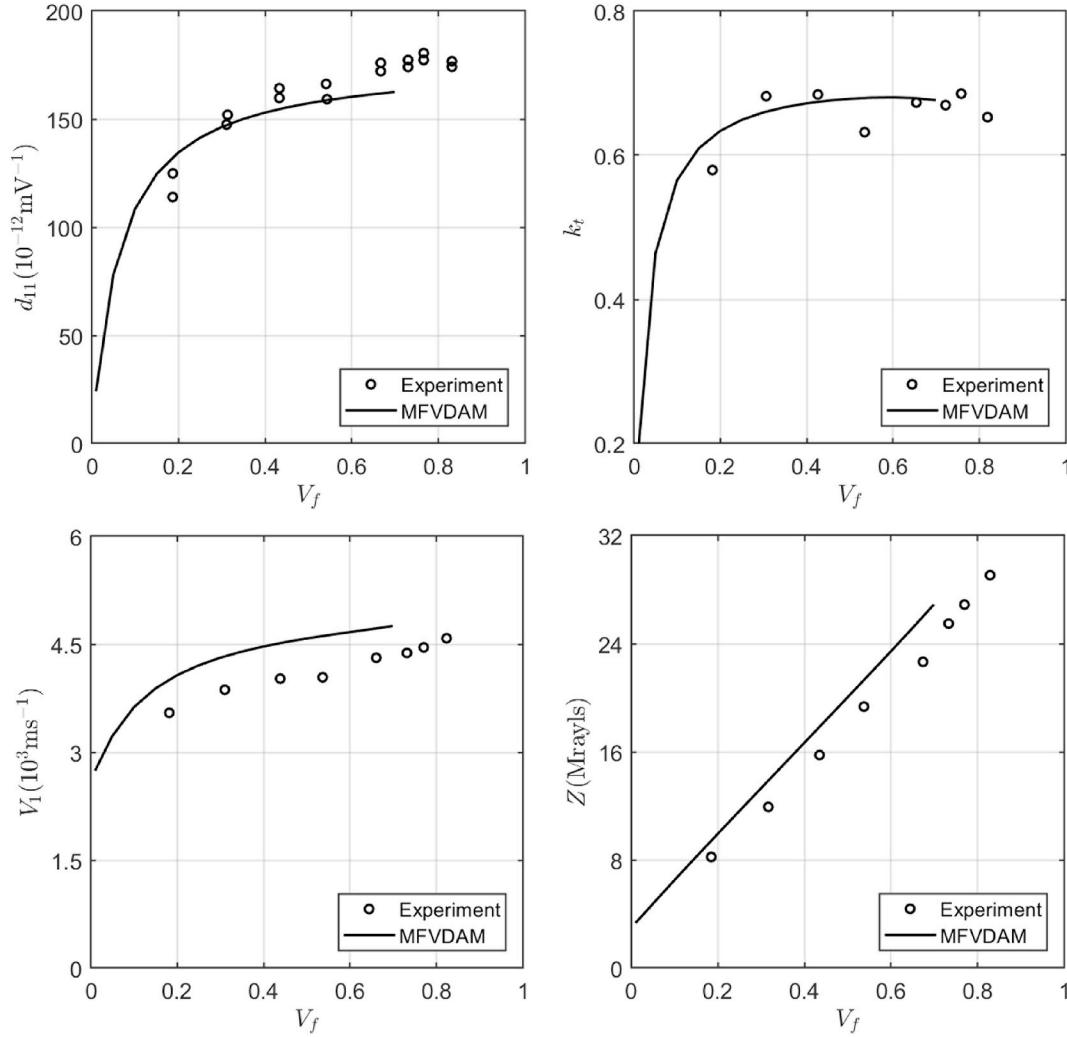
Fig. 13. Comparison of figure of merits generated by the in-house multiphysics FVDAM theory and experimental data (Chan and Unsworth, 1989).

higher-order internal trial functions employed in the finite-element scheme, the convergence of the local fields generated by the MFEM with mesh refinement is faster than that of MFVDAM technique. The MFVDAM technique requires a greater mesh discretization to achieve the same smoothness of the local stress/electric/magnetic fields as those of the MFEM, where the discontinuity of stress/field gradients becomes invisible only for the finest mesh discretization. Nonetheless, the basic characters of the local stress/magnetic/electric fields generated by the MFVDAM are captured with sufficient accuracy even in the case of a coarse mesh (Mesh A), providing additional evidence of the proposed multiphysics FVDAM technique.

In the application of multiphysics composites, the interfacial bonding state plays an important role in affecting the localized responses and hence the homogenized properties of the composites. Based on the credence of the previous simulation, we further investigate the effect of interfacial microcracks on the electrical displacement D_3 distribution of a square unit cell subjected to unit magnetic loading $\bar{B}_2 = 1$ N/Am, Fig. 12. The fiber volume fraction is prescribed as 20%. A pair of symmetric cracks were prescribed along the $\pm 30°$ arc segment of the interface. The continuities of displacements and electric/magnetic potentials are no longer satisfied at the cracked interface. It is observed that the microcracks along the interface significantly affects the internal electric-displacement distributions. Meanwhile, a singular electric field appears at the crack tips, leading to further damage development. The FVDAM results coincide with the FEM prediction, even at the crack tips.

4.3. Experimental verification

Figures of merits are used to assess the utility of piezoelectric composites in specific application scenarios. Various parameters are defined to evaluate the performance of the piezoelectric composites (Chen et al., 2018a):

a) The piezoelectric coupling constant: $k_t = \sqrt{1 - C_{11}^*/\bar{C}_{11}}$, where $\bar{C}_{11} = C_{11}^* + e_{11}^{*2}/\kappa_{11}^*$.
b) The acoustic impedance $Z = \sqrt{\bar{C}_{11}\rho^*}$, where ρ^* is the density of the composite given by $\rho^* = \rho_f V_f + \rho_m(1 - V_f)$, where $\rho_i(i = f, m)$ is the density of either the fiber or matrix phase, Table 1.
c) The longitudinal acoustic velocity is related to material piezoelectricity and density: $V_1 = \sqrt{\bar{C}_{11}/\rho^*}$.
d) The piezoelectric charge coefficient: $d_h = d_{11} + d_{12} + d_{13}$, where $d_{1i} = e_{1j}^* S_{ji}^*$ $(i, j = 1,2,3)$, and S_{ji}^* is the effective compliance component and calculated from $[S^*] = [C^*]^{-1}$.

Fig. 13 compares all of the above four calculated parameters against the experimental data (Chan and Unsworth, 1989) for PZT-7A/Araldite D composites. The elastic and piezoelectric properties of PZT-7A fiber are listed in Table 1 with the density ρ of the PZT-7A prescribed as 7700 kg/m³, while the properties of the isotropic Araldite D matrix are: Young's modulus $E = 4.877$GPa, Poisson's ratio $v = 0.355$, and density $\rho = 1150$kg/m³. It should be noted that the measured value d_{11} for a randomly chosen PZT-7A ceramic is $163–167 \times 10^{-12}$ m/V. Hence,

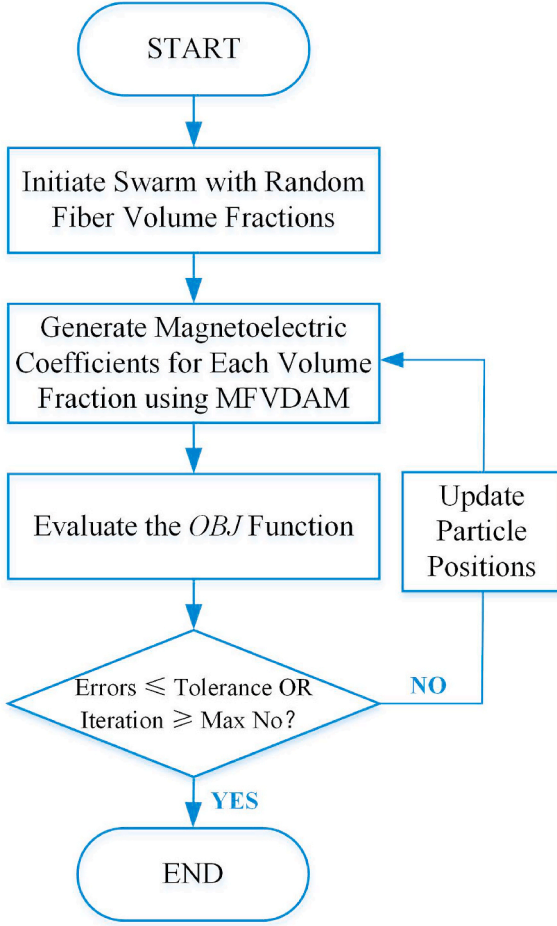**Fig. 14.** Updating algorithm of the MFVDAM-based optimization.

performance of piezoelectric composites. Inspired from Fig. 13, increasing the fiber volume fraction is capable of enhancing the piezoelectric coupling constant k_t until $V_f \leq 0.4$ but with a diminishing rate. In the meantime, the acoustic impedance keeps increasing at almost a constant speed. The observed phenomenon also offers a general idea of designing the multiphysics composites through tailoring the microstructural details (such as fiber volume fraction and constituent properties) to achieve the optimal parameters, which is introduced in the next section.

5. Application

The interaction between magnetism, electricity and elasticity in the unidirectional piezoelectric-piezomagnetic composites produces a unique property that reflects the magnetoelectric coupling effect. This suggests potential usage in magneto-electro-mechanical transducers and sensors. It has been already recognized that the fiber volume fraction has a remarkable influence on the magnetoelectric coupling coefficients of the composites. However, the change of these magnetoelectric coupling coefficients in terms of the fiber volume fraction cannot be described using a simple formula. Herein, the identification of the accurate fiber volume fraction that yields the maximum magnetoelectric coupling coefficients is accomplished by incorporating the MFVDAM theory into the particle swarm optimization algorithm in order to avoid tedious computations in the traditional trial-and-error approach. The MFVDAM-driven particle swarm optimization algorithm facilitates the rapid search of the candidate solutions in all possible fiber volume fraction space via minimizing the objective function:

$$OBJ = \frac{f_1}{|a_{11}^*|} + \frac{f_2}{|a_{22}^*|} + \frac{f_3}{|a_{33}^*|} \tag{28}$$

where f_i are the weights of the three magnetoelectric coupling coefficients. Herein, we set $f_1 = 1, f_2 = f_3 = 0$ because the value of a_{22}^* and a_{33}^* are negligible when compared with the value of a_{11}^*. The magnified a_{11}^* can thus be obtained by minimizing the objective function in Eq. (28).

The particle swarm optimization is advantageous in the sense that it avoids the gradient matrix inversion that could cause numerical instability and instead adopts the concept of social behavior of birds/ants in the process of food search. The general idea is to initiate a group of swarm population whose positions are the initial candidate solutions that will be optimized. For instance, the i-th particle of the population is denoted by its position x_m and moving velocity v_m, respectively. The

$e_{11} = 12.25 \text{C/m}^2$ (which corresponds to $d_{11} = 167 \times 10^{-12}\text{m/V}$) was used in comparison with experimental data. A good agreement is obtained where the experimental data (open circles) are randomly distributed in the vicinity of the generated effective parameters (solid lines). For better engineering applications, a high piezoelectric coupling constant k_t and a low acoustic impedance Z are desired to improve the

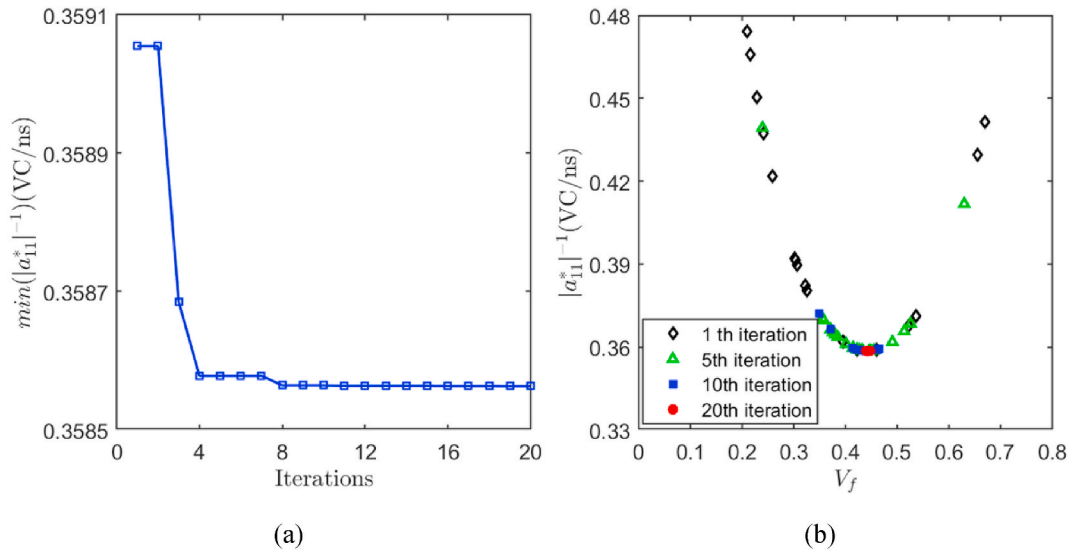(a)   (b)

Fig. 15. Illustration of computational efficiency of the optimization: (a) objective function as a function of iteration numbers and (b) convergence of population after four iteration steps.

initial position of the i-th particle carries the information of the guessed fiber volume fraction. The updating algorithm of the i-th particle at k +1-th iteration is thus expressed as:

$$x_m^{k+1} = x_m^k + v_m^{k+1} \qquad (29)$$

where the moving velocity consists of three components, including its velocity at k-th iteration, the i-th particle's local best experience and the population's global best experience:

$$v_m^{k+1} = \chi[w v_m^k + c_1 \text{rand}()(p_m^k - x_m^k) + c_2 \text{rand}()(g_m^k - x_m^k)] \qquad (30)$$

where p_m^k and g_m^k are the local and global best experiences, respectively. c_1 and c_1 are the acceleration numbers, respectively. rand() is a random number between [0,1]. w is weight factor to constrain the velocity of the last step and is defined in terms of its initial and final values. χ is introduced in Eq. (30) to ensure convergence by tailoring the updating distance.

A group of 15 particles is created within a range between [0,0.75], each particle represents the potential value of the parameter to be optimized – fiber volume fraction. A maximum of 20 iterations is set as the stopping criterion to prevent the ceaseless loop. The detailed updating algorithm is referred to Fig. 14. In this particular situation, we set the error tolerance as 0.01, which is an extremely demanding case, and thus the optimization procedure is continuously updated until the maximum iteration number is reached. A final optimized fiber volume fraction of $V_f|_{optimum} = 0.4429$ is obtained as the magnetoelectric coupling coefficient is magnified to 2.789 $CV^{-1}m^{-1}$ from zeros from both composite phases. Fig. 15 tests the optimization's computational efficiency by generating the objective function as a function of iteration numbers and illustrating the population's locations after several different iteration steps. It is seen that the optimization is almost converged to a value of $OBJ = 0.3586$ after the fourth iteration, which is also proved by Fig. 15(b) where a few particles already reach the lowest point after the 5-th iteration and all particles converge to the same point after the final iteration.

6. Summary and conclusions

The 0-th order finite volume direct averaging micromechanics is extended with fully coupled piezoelectric-pizeomagnetic capabilities to simulate the effective and localized responses of periodic unidirectional composites. For composites with generalized constituents, the present theory admits fully anisotropic material constitutive relationship for subvolumes. The repeating unit cells (RUCs) with square or hexagonal geometry are adopted to mimic different fiber arrangements. The present MFVDAM theory is validated against the in-house higher-order finite elements and generalized Eshelby technique. The computational efficiency of the MFVDAM is tested by directly comparing against the in-house MFEM in the effort of implementing mesh discretization, stiffness matrix densities as well as the execution time. It is concluded that the present MFVDAM can significantly enhance the computational effort without sacrificing accuracy. We also conclude that the electromagnetic coupling coefficients can be generated by combining pure piezoelectric and piezomagnetic constituents, which offers more flexible options in the design of electric-magnetic conversion micromachines.

Declaration of competing interest

The authors declare that they have no known competing financial interests or personal relationships that could have appeared to influence the work reported in this paper.

Acknowledgement

References

Ameen, M.M., Peerlings, R.H.J., Geers, M.G.D., 2018. A quantitative assessment of the scale separation limits of classical and higher-order asymptotic homogenization. Eur. J. Mech. Solid. 71, 89–100.

Benveniste, Y., 1994. On the micromechanics of fibrous piezoelectric composites. Mech. Mater. 18, 183–193.

Bishay, P.L., Atluri, S.N., 2015. Computational Piezo-Grains (CPGs) for a highly-efficient micromechanical modeling of heterogeneous piezoelectric–piezomagnetic composites. Eur. J. Mech. Solid. 53, 311–328.

Bishay, P.L., Dong, L., Atluri, S.N., 2014. Multi-physics computational grains (MPCGs) for direct numerical simulation (DNS) of piezoelectric composite/porous materials and structures. Comput. Mech. 54, 1129–1139.

Cavalcante, M.A., Marques, S.P., Pindera, M.-J., 2007. Parametric Formulation of the Finite-Volume Theory for Functionally Graded Materials—Part I: Analysis.

Chan, H.L.W., Unsworth, J., 1989. Simple model for piezoelectric ceramic/polymer 1-3 composites used in ultrasonic transducer applications. IEEE Trans. Ultrason. Ferroelectrics Freq. Contr. 36, 434–441.

Chen, Q., Pindera, M.-J., 2020. Homogenization and localization of elastic-plastic nanoporous materials with Gurtin-Murdoch interfaces: an assessment of computational approaches. Int. J. Plast. 124, 42–70.

Chen, Q., Tu, W., Liu, R., Chen, X., 2018a. Parametric multiphysics finite-volume theory for periodic composites with thermo-electro-elastic phases. J. Intell. Mater. Syst. Struct. 29, 530–552.

Chen, Q., Wang, G., 2018. Homogenized and localized responses of coated magnetostrictive porous materials and structures. Compos. Struct. 187, 102–115.

Chen, Q., Wang, G., 2020. Computationally-efficient homogenization and localization of unidirectional piezoelectric composites with partially cracked interface. Compos. Struct. 232, 111452.

Chen, Q., Wang, G., Chen, X., 2018b. Three-dimensional parametric finite-volume homogenization of periodic materials with multi-scale structural applications. International Journal of Applied Mechanics 10, 1850045.

Chen, Q., Wang, G., Pindera, M.-J., 2018c. Homogenization and localization of nanoporous composites-A critical review and new developments. Compos. B Eng. 155, 329–368.

Chen, Q., Wang, G., Pindera, M.-J., 2018d. Homogenization and localization of nanoporous composites - a critical review and new developments. Compos. B Eng. 155, 329–368.

Dinzart, F., Sabar, H., 2011. Magneto-electro-elastic coated inclusion problem and its application to magnetic-piezoelectric composite materials. Int. J. Solid Struct. 48, 2393–2401.

Espinosa-Almeyda, Y., Camacho-Montes, H., Rodríguez-Ramos, R., Guinovart-Díaz, R., López-Realpozo, J., Bravo-Castillero, J., Sabina, F., 2017. Influence of imperfect interface and fiber distribution on the antiplane effective magneto-electro-elastic properties for fiber reinforced composites. Int. J. Solid Struct. 112, 155–168.

Gattu, M., Khatam, H., Drago, A.S., Pindera, M.-J., 2008. Parametric finite-volume micromechanics of uniaxial continuously-reinforced periodic materials with elastic phases. J. Eng. Mater. Technol. 130.

Haghgoo, M., Ansari, R., Hassanzadeh-Aghdam, M., Darvizeh, A., 2019. Fully coupled thermo-magneto-electro-elastic properties of unidirectional smart composites with a piezoelectric interphase. Proc. IME C J. Mech. Eng. Sci. 233, 2813–2829.

Hasanzadeh, M., Ansari, R., Hassanzadeh-Aghdam, M., 2019. Evaluation of effective properties of piezoelectric hybrid composites containing carbon nanotubes. Mech. Mater. 129, 63–79.

He, Z., Pindera, M.-J., 2020. Locally exact asymptotic homogenization of periodic materials under anti-plane shear loading. Eur. J. Mech. Solid. 81, 103972.

Jiang, C., Cheung, Y., 2001. An exact solution for the three-phase piezoelectric cylinder model under antiplane shear and its applications to piezoelectric composites. Int. J. Solid Struct. 38, 4777–4796.

Khatam, H., Pindera, M.-J., 2009. Parametric finite-volume micromechanics of periodic materials with elastoplastic phases. Int. J. Plast. 25, 1386–1411.

Kuo, H.-Y., 2014. Fibrous composites of piezoelectric and piezomagnetic phases: generalized plane strain with transverse electromagnetic fields. Mech. Mater. 75, 103–110.

Kuo, H.-Y., Peng, C.-Y., 2013. Magnetoelectricity in coated fibrous composites of piezoelectric and piezomagnetic phases. Int. J. Eng. Sci. 62, 70–83.

Lee, J., Boyd IV, J.G., Lagoudas, D.C., 2005. Effective properties of three-phase electromagneto-elastic composites. Int. J. Eng. Sci. 43, 790–825.

Li, J.Y., Dunn, M.L., 1998. Micromechanics of magnetoelectroelastic composite materials: average fields and effective behavior. J. Intell. Mater. Syst. Struct. 9, 404–416.

Munalli, D., Dimitrakis, G., Chronopoulos, D., Greedy, S., Long, A., 2019. Electromagnetic shielding effectiveness of carbon fibre reinforced composites. Compos. B Eng. 173, 106906.

Rabczuk, T., Ren, H., Zhuang, X., 2019. A nonlocal operator method for partial differential equations with application to electromagnetic waveguide problem. Comput. Mater. Continua (CMC) 59 (2019) Nr. 1.

Rashidinejad, E., Shodja, H., 2019. On the exact nature of the coupled-fields of magneto-electro-elastic ellipsoidal inclusions with non-uniform eigenfields and general anisotropy. Mech. Mater. 128, 89–104.

Sladek, J., Sladek, V., Repka, M., Kasala, J., Bishay, P., 2017. Evaluation of effective material properties in magneto-electro-elastic composite materials. Compos. Struct.

174, 176–186.

Tang, T., Yu, W., 2009. Micromechanical modeling of the multiphysical behavior of smart materials using the variational asymptotic method. Smart Mater. Struct. 18, 125026.

Tong, Z., Lo, S., Jiang, C., Cheung, Y., 2008. An exact solution for the three-phase thermo-electro-magneto-elastic cylinder model and its application to piezoelectric–magnetic fiber composites. Int. J. Solid Struct. 45, 5205–5219.

Vijay, S., Tugirumubano, A., Go, S.H., Kwac, L.K., Kim, H.G., 2018. Numerical simulation and experimental validation of electromagnetic properties for Al-MWCNT-Fe2O3 hybrid nano-composites. J. Alloys Compd. 731, 465–470.

Wang, G., 2018. Homogenized and localized stress reconfigurations of solid or hollow fiber reinforced materials in a multi-scale framework. Compos. Struct. 184,

1099–1110.

Xu, X., Qing, A., Gan, Y., Feng, Y., 2007. An experimental study on electromagnetic properties of random fiber composite materials. Microw. Opt. Technol. Lett. 49, 185–190.

Yang, H., Abali, B.E., Timofeev, D., Müller, W.H., 2019. Determination of metamaterial parameters by means of a homogenization approach based on asymptotic analysis. Continuum Mech. Therm. 1–20.

Zhu, J., Bettaieb, M.B., Abed-Meraim, F., 2020. Numerical investigation of necking in perforated sheets using the periodic homogenization approach. Int. J. Mech. Sci. 166, 105209.